Supporting Information for:

Understanding the Evolution of Double Perovskite Band Structure upon Dimensional Reduction

Bridget A. Connor,[a] Alexander C. Su,[a] Adam H. Slavney,[a] Linn Leppert,*[,b] and Hemamala I. Karunadasa*[a,c]

[a] Department of Chemistry, Stanford University, Stanford, CA 94305, USA.
[b] MESA+ Institute for Nanotechnology, University of Twente, 7500 AE Enschede, The Netherlands.
[c] Stanford Institute for Materials and Energy Sciences, SLAC National Accelerator Laboratory, Menlo Park, CA 94025, USA.
*hemamala@stanford.edu, l.leppert@utwente.nl

Table of contents:

S1 General notes **1**
S2 Computational Methods **1**
S3 Derivation of σ-bonding SALCs **2**
S3.1 The *n* = 1 case 2
S3.2 The *n* = 2 case 3
S4 Effects of spin-orbit coupling (SOC) on the conduction bands of the Ag–Bi double perovskites **5**
S5 LCAO analysis of 2D Ag–Tl perovskites **6**
S5.1 The *n* = 1 Ag–Tl structure 6
S5.1.1 Predictions for the valence band *6*
S5.1.2 Predictions for the conduction band *8*
S5.1.3 Comparison of predictions to DFT calculations *8*
S5.2 The *n* = 2 Ag–Tl structure 8
S5.2.1 Predictions for the valence band *8*
S5.2.2 Predictions for the conduction band *10*
S5.2.3 Comparison of predictions to DFT calculations *10*
S5.3 Contributions of Tl d orbitals to the VB 11
S6 Extending the LCAO analysis to π-bonding states **12**
S6.1 Derivation of selected π-bonding SALCs and Bloch waves for the *n* = 1 case 13
S6.2 The axial and equatorial effects for dxy, dxz, and dyz bands 14
S6.3 3D vs 2D translational symmetry: effects on the dxy, dxz, and dyz bands 15
S6.3.1 Example 1: The dxy band *16*
S6.3.2 Example 2: The dyz/dxz bands *16*
S6.4 A note of caution in analyzing π-bonding states in the 2D case 17
S6.5 The A_{2g}-derived band 18

S7 Analogy between 3D and 2D halide SALCs and splitting of the 3D T_{1u} SALCs at the X point and in the 2D case 18

S8 A note on d orbital contributions from the B′ cation 20

S9 Bands with no metal orbital participation 20

S10 Additional Figures 21

S1 General notes

In all figures, brown circles represent halide atoms with yellow and white lobes to represent their p orbitals. Gray, orange, and purple circles represent B or B′ site cations with gray and white shapes representing their frontier orbitals where relevant. Yellow shading of p orbital lobes and gray shading of metal orbital lobes represent positive phases, while white shading of either represents negative phases. Unless otherwise specified, the relative size of halide p orbital lobes is kept uniform for simplicity. All DFT band structures are shown in duplicate where orbital contributions from the two different metal cations are plotted separately in the left and right panels as colored dots. Abbreviations used: VB = valence band, CB = conduction band, VBM = valence band maximum, CBM = conduction band minimum, LCAO = linear combination of atomic orbitals, SALC = symmetry adapted linear combination, MO = molecular orbital, HOMO = highest occupied molecular orbital, LUMO = lowest unoccupied molecular orbital, DFT = density functional theory.

S2 Computational Methods

Our first principles density functional theory (DFT) calculations were performed using the Vienna Ab Initio Simulation Package (VASP).[1, 2] We started by fully relaxing the structures of all studied 3D double perovskites using the exchange-correlation approximation PBEsol.[3] The Brillouin zone integrations were performed on a grid of 4×4×4 *k*-points, with a cutoff energy for the plane wave expansion of 600 eV. Forces were relaxed until smaller than 0.0001 eV/ Å. Projector Augmented Wave (PAW) potentials[4] were used with the following valence configurations: Cs: $5s^2 5p^6 6s^1$, Ag: $4d^{10} 5s^1$, Sb: $5s^2 5p^3$, Bi: $6s^2 6p^3$, Tl: $6s^2 6p^1$, Br: $4s^2 4p^5$. We then used the relaxed structures to construct model mono- (n = 1) and bilayers (n = 2) of each double perovskite. Spurious interactions between periodic images were avoided by separating the double perovskite layers by a vacuum layer of ~ 30 Å and by using dipole corrections in all calculations.

For the band structure calculations, we used a plane wave energy cutoff of 500 eV and included spin-orbit coupling self-consistently. We used PBEsol for all band structures apart from that of $Cs_2AgTlBr_6$ and the corresponding mono- and bilayer structures because PBEsol erroneously predicts $Cs_2AgTlBr_6$ to be metallic. For $Cs_2AgTlBr_6$, we used a 6×6×6 *k*-point grid and a modified version of the PBE0 functional with 35% of exact exchange, chosen to reproduce the experimental band gap of this compound. The band structures of the mono- and bilayer model structures were also calculated using PBE0 with 35% of exact exchange. Since the band gap of $Cs_2AgTlBr_6$ is not affected by spin-orbit interactions, we did not include it in our band structure calculations of $Cs_2AgTlBr_6$ and the corresponding mono- and bilayer.

For the electronic structure calculations of the monolayer (bilayer) structures, we used a 4×4×1(2) *k*-point grid. Atomic orbital contributions at each *k*-point were obtained by projecting DFT orbitals onto spherical harmonics within spheres centered at each ion.

S3 Derivation of σ-bonding SALCs

S3.1 The $n = 1$ case

We will construct σ-bonding SALCs for the $[BX_6]^{n-}$ root MO of an $n = 1$ structure by considering the σ-bonding p orbitals on the six halide atoms surrounding the B site. Due to the inequivalence of the terminal axial halides and the bridging equatorial halides, this configuration of p orbitals has D_{4h} symmetry, which is a lower symmetry than could be applied in the 3D case (O_h) where all halides are equivalent. Labels for the six σ-bonding halide p orbitals are defined in Figure S1A and the different colors of the orbital lobes denote symmetry equivalent halide orbitals. We generate two reducible representations ($\Gamma_{1,2}$ and $\Gamma_{3\text{-}6}$, Figure S1B), one for each set of symmetry related p orbitals, by tracking how many orbitals in each set are unaltered by each symmetry operation. By consulting the D_{4h} character table, we decompose $\Gamma_{1,2}$ and $\Gamma_{3\text{-}6}$ into irreducible representations, finding that $\Gamma_{1,2} \rightarrow A_{1g} + A_{2u}$ and $\Gamma_{3\text{-}6} \rightarrow A_{1g} + B_{1g} + E_u$.

We can now apply the method of projection operators to construct halide SALCs according to the symmetry defined by these irreducible representations. Projection tables for one p orbital from each symmetry-related set are given in Figure S1C. These tables track a starting halide p orbital (φ_x) through the various symmetry operations of the D_{4h} point group and list which p orbital (φ_i) it is mapped onto by each operation (for example, the two dihedral mirror planes (σ_d) map φ_3 onto φ_4 and φ_6). Using these tables, we can easily apply the projection operator, which is defined as:

$$\boldsymbol{P}_{\boldsymbol{\Gamma_{irr.}}}(\varphi_x) = \frac{1}{N}\sum \chi_j \times \varphi_j$$

Thus, we multiply each p orbital (φ_j) that results from applying a given symmetry operation to the starting p orbital (φ_x) by the character of that symmetry operation under the irreducible representation $\Gamma_{irr.}$ (χ_j). We then repeat this for all symmetry operations and sum the resulting terms, arriving at a SALC with Γ_{irr} symmetry. This SALC is normalized by a factor N (defined below, c_x is the coefficient for each φ_j after application of the projection operator).

$$N = \sqrt{\sum (c_x)^2}$$

In some cases, it is appropriate to take linear combinations of several SALCs of the same symmetry to generate a final SALC that can fully interact with a metal orbital (or a set of degenerate metal orbitals) of matching symmetry. Since we cannot quantitatively determine the relative contributions of these two A_{1g}

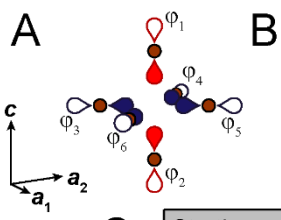

B

D_{4h}	E	$2C_4(z)$	C_2	$2C_2'$	$2C_2''$	i	$2S_4$	σ_h	$2\sigma_v$	$2\sigma_d$	$\Gamma_{irreducible}$
$\Gamma_{1,2}$	2	2	2	0	0	0	0	0	2	2	$A_{1g} + A_{2u}$
$\Gamma_{3\text{-}6}$	4	0	0	2	0	0	0	4	2	0	$A_{1g} + B_{1g} + E_u$

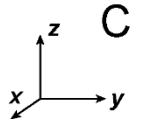

Starting orbital:	E	$2C_4(z)$	C_2	$2C_2'$	$2C_2''$	i	$2S_4$	σ_h	$2\sigma_v$	$2\sigma_d$
φ_1	φ_1	$2\varphi_1$	φ_1	$2\varphi_2$	$2\varphi_2$	φ_2	$2\varphi_2$	φ_2	$2\varphi_1$	$2\varphi_1$
φ_3	φ_3	φ_4, φ_6	φ_5	$2\varphi_3$	φ_4, φ_6	φ_5	φ_4, φ_6	φ_3	φ_3, φ_5	φ_4, φ_6

Figure S1. Derivation of σ-bonding SALCs for the undistorted $n = 1$ structure. (A) The D_{4h}-symmetric arrangement of the σ-bonding halide p orbitals around the B site. Sets of symmetry related orbitals are drawn in the same color. (B) Reducible representations for the two sets of symmetry-related p orbitals and their decomposition into irreducible representations. (C) Projection table for the φ_1 and φ_3 orbitals.

SALCs without detailed electronic structure calculations, in this work, we choose contributions that generate SALCs that match the 3D O_h SALCs.

We found above that both $\Gamma_{1,2}$ and $\Gamma_{3\text{-}6}$ have an irreducible representation of A_{1g} symmetry. Applying the projection operator to one starting halide orbital from each set gives:

$$\boldsymbol{P}_{\boldsymbol{A_{1g}}}(\varphi_1) = \frac{1}{\sqrt{2}}(\varphi_1 + \varphi_2)$$

$$\boldsymbol{P}_{\boldsymbol{A_{1g}}}(\varphi_3) = \frac{1}{2}(\varphi_3 + \varphi_4 + \varphi_5 + \varphi_6)$$

We can then take linear combinations of these two A_{1g} SALCs to generate new SALCs ($A_{1g}^{(s)}$ and $A_{1g}^{(d)}$) that involve all six halide p orbitals. We choose coefficients that match the 3D O_h SALCs, noting that our qualitative predictions for all n = 1 systems discussed are safely preserved as long as there is at least equal contribution from the axial halides compared to the equatorial halides in the final $A_{1g}^{(d)}$ SALC. These are the SALCs given in main text Figure 3.

$$\boldsymbol{A_{1g}^{(s)}}: \frac{1}{\sqrt{3}}\boldsymbol{P}_{\boldsymbol{A_{1g}}}(\varphi_1) + \frac{\sqrt{2}}{\sqrt{3}}\boldsymbol{P}_{\boldsymbol{A_{1g}}}(\varphi_3) = \frac{1}{\sqrt{6}}(\varphi_1 + \varphi_2 + \varphi_3 + \varphi_4 + \varphi_5 + \varphi_6)$$

$$\boldsymbol{A_{1g}^{(d)}}: \frac{\sqrt{2}}{\sqrt{3}}\boldsymbol{P}_{\boldsymbol{A_{1g}}}(\varphi_1) - \frac{1}{\sqrt{3}}\boldsymbol{P}_{\boldsymbol{A_{1g}}}(\varphi_3) = \frac{1}{2\sqrt{3}}(2\varphi_1 + 2\varphi_2 - \varphi_3 - \varphi_4 - \varphi_5 - \varphi_6)$$

The B_{1g} and A_{2u} SALCs can be determined by applying the projection operator to φ_3 and φ_1, respectively. These SALCs are pictured in main text Figure 3.

$$\boldsymbol{B_{1g}}: \boldsymbol{P}_{\boldsymbol{B_{1g}}}(\varphi_3) = \frac{1}{2}(\varphi_3 - \varphi_4 + \varphi_5 - \varphi_6)$$

$$\boldsymbol{A_{2u}}: \boldsymbol{P}_{\boldsymbol{A_{2u}}}(\varphi_1) = \frac{1}{\sqrt{2}}(\varphi_1 - \varphi_2)$$

Applying the projection operator according to the E_u irreducible representation to φ_3 gives a SALC involving only two of the equatorial halide atoms. We obtain a second unique SALC by operating on φ_4.

$$\boldsymbol{P}_{\boldsymbol{E_u}}(\varphi_3) = \frac{1}{\sqrt{2}}(\varphi_3 - \varphi_5)$$

$$\boldsymbol{P}_{\boldsymbol{E_u}}(\varphi_4) = \frac{1}{\sqrt{2}}(\varphi_4 - \varphi_6)$$

Taking linear combinations of these two E_u SALCs (with coefficients that assume equal participation from each) yields new SALCs that incorporate all four equatorial p orbitals. These are the SALCs given in main text Figure 3.

$$\boldsymbol{E_u^{(1)}}: \frac{1}{\sqrt{2}}\boldsymbol{P}_{\boldsymbol{E_u}}(\varphi_3) + \frac{1}{\sqrt{2}}\boldsymbol{P}_{\boldsymbol{E_u}}(\varphi_4) = \frac{1}{2}(\varphi_3 + \varphi_4 - \varphi_5 - \varphi_6)$$

$$\boldsymbol{E_u^{(2)}}: \frac{1}{\sqrt{2}}\boldsymbol{P}_{\boldsymbol{E_u}}(\varphi_3) - \frac{1}{\sqrt{2}}\boldsymbol{P}_{\boldsymbol{E_u}}(\varphi_4) = \frac{1}{2}(\varphi_3 - \varphi_4 - \varphi_5 + \varphi_6)$$

S3.2 The n = 2 case

We will construct σ-bonding SALCs for the $[BX_6]^{n-}$ root MO of an $n = 2$ structure by considering the σ-bonding p orbitals on the six halide atoms surrounding the B site. The symmetry of this configuration is further lowered from that found in the $n = 1$ structure due to the inequivalence of the two axial halide atoms: one is terminal whereas the other is bridging. The appropriate point group is therefore C_{4v}. Labels for the six σ-bonding halide p orbitals are defined in Figure S2A and the different colors of the orbital lobes denote those halide orbitals that are related by symmetry. We generate three reducible representations (Γ_1 Γ_2, and $\Gamma_{3\text{-}6}$, Figure S2B), one for each set of symmetry related p orbitals, by tracking how many orbitals in each set are unaltered by each symmetry operation. By consulting the C_{4v} character table, we decompose Γ_1, Γ_2, and $\Gamma_{3\text{-}6}$ into irreducible representations finding that Γ_1 and $\Gamma_2 \rightarrow A_1$ and $\Gamma_{3\text{-}6} \rightarrow A_1 + B_1 + E$.

We use the projection operator (as outlined above) to construct halide SALCs according to the symmetry defined by these irreducible representations. Projection tables for one p orbital from each symmetry-related set (φ_1, φ_2, and φ_3) are given in Figure S2C.

Γ_1, Γ_2, and $\Gamma_{3\text{-}6}$ all reduce to give an irreducible representation of A_1 symmetry. Applying the projection operator to one halide orbital from each set gives:

$$\boldsymbol{P}_{\boldsymbol{A_1}}(\varphi_1) = \varphi_1$$

$$\boldsymbol{P}_{\boldsymbol{A_1}}(\varphi_2) = \varphi_2$$

$$\boldsymbol{P}_{\boldsymbol{A_1}}(\varphi_3) = \frac{1}{2}(\varphi_3 + \varphi_4 + \varphi_5 + \varphi_6)$$

We can then take linear combinations of these three A_1 SALCs to generate new SALCs capable of fully interacting with B-site s, dz^2, and p_z orbitals. Similar to the $n = 1$ case, we choose coefficients that yield $A_1^{(s)}$ and $A_1^{(d)}$ SALCs that are directly analogous to the 3D A_1 and $E_g^{(1)}$ SALCs. For the $A_1^{(p)}$ SALC, we assume equal participation from the two basis SALCs involved. These are the SALCs given in main text Figure 3.

$$\boldsymbol{A_1^{(s)}}: \frac{\boldsymbol{1}}{\sqrt{\boldsymbol{6}}}\boldsymbol{P}_{\boldsymbol{A_1}}(\varphi_1) + \frac{\boldsymbol{1}}{\sqrt{\boldsymbol{6}}}\boldsymbol{P}_{\boldsymbol{A_1}}(\varphi_2) + \frac{\sqrt{\boldsymbol{2}}}{\sqrt{\boldsymbol{3}}}\boldsymbol{P}_{\boldsymbol{A_1}}(\varphi_3) = \frac{1}{\sqrt{6}}(\varphi_1 + \varphi_2 + \varphi_3 + \varphi_4 + \varphi_5 + \varphi_6)$$

A

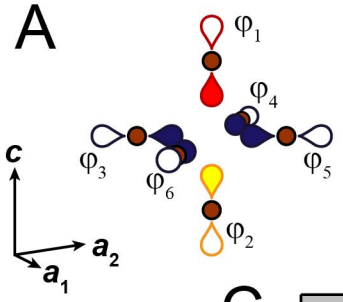

B

C_{4v}	E	$2C_4(z)$	C_2	$2\sigma_v$	$2\sigma_d$	$\Gamma_{irreducible}$
Γ_1	1	1	1	1	1	A_1
Γ_2	1	1	1	1	1	A_1
$\Gamma_{3\text{-}6}$	4	0	0	2	0	$A_1 + B_1 + E$

C

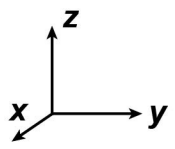

Starting orbital:	E	$2C_4(z)$	C_2	$2\sigma_v$	$2\sigma_d$
φ_1	φ_1	$2\varphi_1$	φ_1	$2\varphi_1$	$2\varphi_1$
φ_2	φ_2	$2\varphi_2$	φ_2	$2\varphi_2$	$2\varphi_2$
φ_3	φ_3	φ_4, φ_6	φ_5	φ_3, φ_5	φ_4, φ_6

Figure S2. Derivation of σ-bonding SALCs for the undistorted $n = 2$ structure. (A) The C_{4v}-symmetric arrangement of the σ-bonding halide p orbitals around the B site. Sets of symmetry related orbitals are drawn in the same color. (B) Reducible representations for the three sets of symmetry-related p orbitals and their decomposition into irreducible representations. (C) Projection table for the φ_1, φ_2, and φ_3 orbitals.

$$\boldsymbol{A_1^{(d)}}: \frac{\mathbf{1}}{\sqrt{\mathbf{3}}}\boldsymbol{P_{A_1}}(\varphi_1) + \frac{\mathbf{1}}{\sqrt{\mathbf{3}}}\boldsymbol{P_{A_1}}(\varphi_2) - \frac{1}{\sqrt{3}}\boldsymbol{P_{A_1}}(\varphi_3) = \frac{1}{2\sqrt{3}}(2\varphi_1 + 2\varphi_2 - \varphi_3 - \varphi_4 - \varphi_5 - \varphi_6)$$

$$\boldsymbol{A_1^{(p)}}: \frac{\mathbf{1}}{\sqrt{\mathbf{2}}}\boldsymbol{P_{A_1}}(\varphi_1) - \frac{\mathbf{1}}{\sqrt{\mathbf{2}}}\boldsymbol{P_{A_1}}(\varphi_2) = \frac{1}{\sqrt{2}}(\varphi_1 - \varphi_2)$$

The B_1 SALC can be determined by applying the projection operator to φ_3. This SALC is pictured in main text Figure 3.

$$\boldsymbol{B_1}: \boldsymbol{P_{B_1}}(\varphi_3) = \frac{1}{2}(\varphi_3 - \varphi_4 + \varphi_5 - \varphi_6)$$

As in the $n = 1$ case, we obtain two unique E SALCs by applying the projection operator to φ_3 and φ_4.

$$\boldsymbol{P_E}(\varphi_3) = \frac{1}{\sqrt{2}}(\varphi_3 - \varphi_5)$$

$$\boldsymbol{P_E}(\varphi_4) = \frac{1}{\sqrt{2}}(\varphi_4 - \varphi_6)$$

Taking linear combinations of these two E SALCs (with coefficients that assume equal participation from each) yields new SALCs that incorporate all four equatorial p orbitals. These are the SALCs given in main text Figure 3.

$$\boldsymbol{E^{(1)}}: \frac{1}{\sqrt{2}}\boldsymbol{P_E}(\varphi_3) + \frac{1}{\sqrt{2}}\boldsymbol{P_E}(\varphi_4) = \frac{1}{2}(\varphi_3 + \varphi_4 - \varphi_5 - \varphi_6)$$

$$\boldsymbol{E^{(2)}}: \frac{1}{\sqrt{2}}\boldsymbol{P_E}(\varphi_3) - \frac{1}{\sqrt{2}}\boldsymbol{P_E}(\varphi_4) = \frac{1}{2}(\varphi_3 - \varphi_4 - \varphi_5 + \varphi_6)$$

S4 Effects of spin-orbit coupling (SOC) on the conduction bands of the Ag–Bi double perovskites

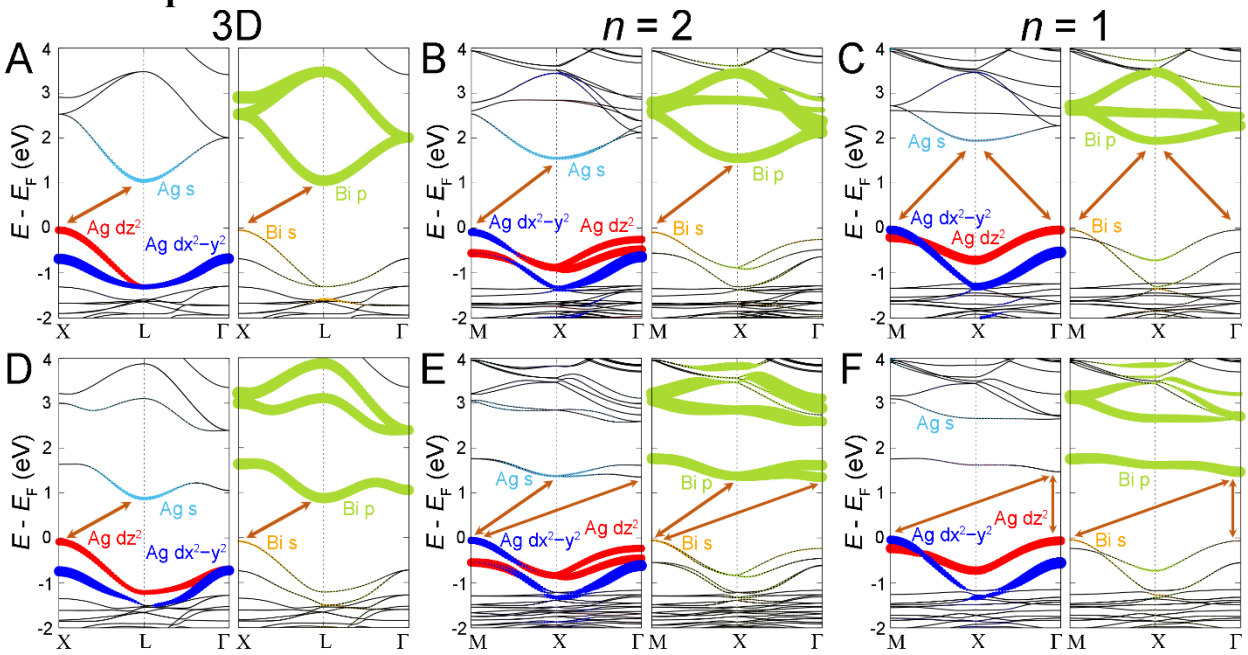

Figure S3. DFT band structures of 3D $Cs_2AgBiBr_6$ and the undistorted $n = 2$ and $n = 1$ Ag–Bi derivatives calculated without SOC (A, B, and C, respectively) and with SOC (D, E, and F, respectively). Including SOC significantly changes the CB dispersion of the $n = 1$ structure.

SOC has a substantial effect on the dispersion pattern of the Bi 6p-derived CB of $Cs_2AgBiBr_6$ and its layered derivatives (Figure S3). Since the analysis presented here is a non-relativistic one, which does not account for SOC effects, an analysis of these changes is beyond the scope of this work. Nevertheless, it is important to point out that in the undistorted model n = 1 Ag–Bi double perovskite, SOC moves the CBM to Γ. As previously reported, this generates a direct bandgap at Γ since this change is accompanied by a simultaneous shifting of the VBM to Γ due to 2D translational symmetry and the axial effect (main text Section 3.2.2).

It is worth pointing out that SOC does not have such a substantial effect on the band structure of $Cs_2AgSbBr_6$ and its layered derivatives where Sb 5p orbitals make up the CB. This is because SOC, which is a relativistic effect, has a smaller impact on Sb 5p orbitals than on Bi 6p orbitals. Here, the bandgap symmetry is unaffected by the inclusion of SOC (Figure S4) and also remains unchanged as the 3D lattice is reduced to the monolayer limit, despite the change in the VB dispersion pattern from the 3D to the 2D lattice (main text Section 3.2.3).

S5 LCAO analysis of 2D Ag–Tl perovskites

S5.1 The *n* = 1 Ag–Tl structure

S5.1.1 Predictions for the valence band

Like $Cs_2AgBiBr_6$, the root MOs of the two highest energy VBs of $Cs_2AgTlBr_6$ are the antibonding combinations of the Ag dz^2 and $dx^2–y^2$ orbitals with the halide SALCs of matching symmetry. Thus, to map out the dispersion pattern of the VB of the Ag–Tl n = 1 structure, we will consider the same sets of $A_{1g}^{(d)}$- and B_{1g}-derived Bloch waves as for the Ag–Bi n = 1 structure considered in main text Section 2.3.1. However, the dispersion pattern of the resulting bands will differ from the Ag–Bi case because the frontier orbitals of Tl^{3+} are not the same as those of Bi^{3+}, leading to different interactions at the B′ site. The HOMOs of Tl^{3+} (the dz^2 and $dx^2–y^2$ orbitals) are expected to make only small contributions to the VB, which will be neglected in the following analysis (see Section S5.3 for justification). Thus, we rank the $A_{1g}^{(d)}$- and B_{1g}-derived Bloch waves based solely on the 90° X-X interactions present at the B′ site. This results in the

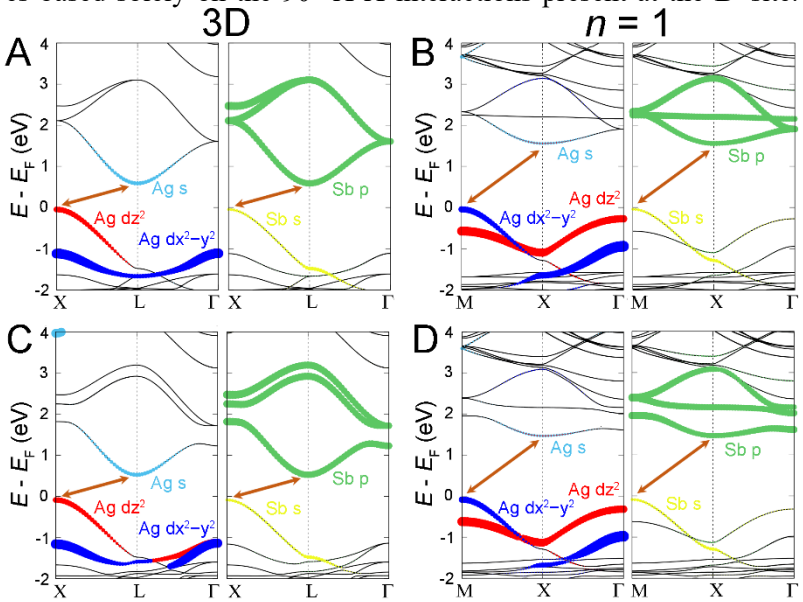

Figure S4. DFT band structures of 3D $Cs_2AgSbBr_6$ and the undistorted n = 1 Ag–Sb derivative calculated without SOC (A and B, respectively) and with SOC (C and D, respectively). Including SOC has no major consequences for the band structure.

energetic ordering Γ < X < M for the dz^2 band and M < X < Γ for the $dx^2–y^2$ band (Figure S5A-F). In contrast to the Ag–Bi system, here, an in-phase arrangement of halide p orbitals at the B′ site represents a stabilizing interaction (due to the bonding 90° X-X interactions) rather than a destabilizing one, since no B′ metal s orbital is available to form antibonding interactions. However, similar to the Ag–Bi case, the equatorial effect leads us to predict that the 90° X-X antibonding interactions at the B′ site will be stronger in the $dx^2–y^2$ band at Γ (Figure S5F) than in the dz^2 band at M (Figure S5C). Thus, we expect greater

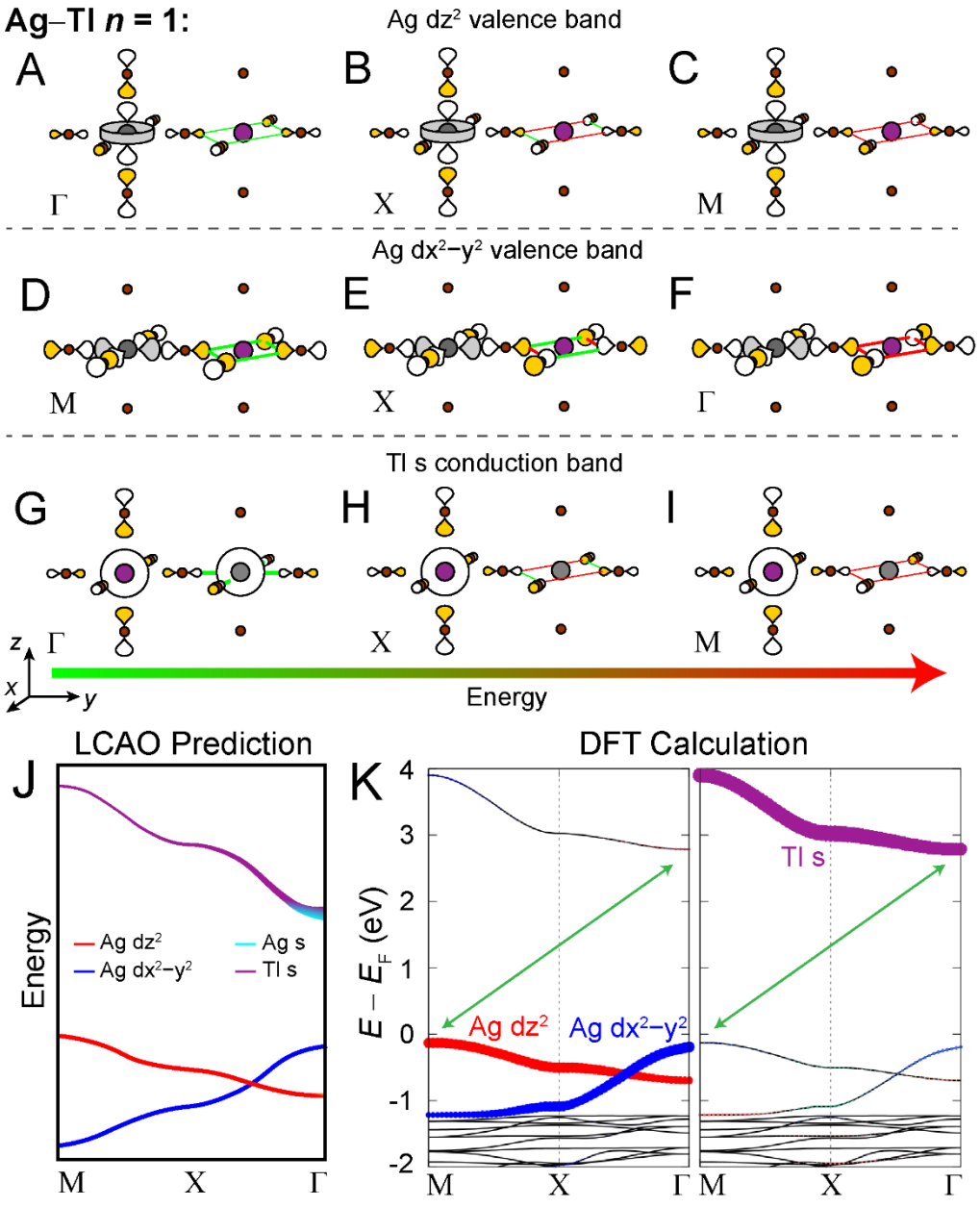

Figure S5. LCAO depictions of the Ag dz^2 (A-C), Ag $dx^2–y^2$ (D-F), and Tl s (G-I) bands of the Ag–Tl n = 1 structure at the M, X, and Γ points ranked in order of increasing energy from left to right. The bonding and antibonding interactions at the B′ site are shown as green and red lines, respectively, and the thickness of each line corresponds to the strength of the interaction. Halide p orbital lobes are scaled to represent approximate relative electron densities. (J) Predicted band diagram of the n = 1 Ag–Tl structure. (K) DFT band structure of the n = 1 Ag–Tl structure. Gray and purple spheres represent Ag and Tl atoms, respectively.

dispersion along the X→Γ direction in the dx^2-y^2 band than along the X→M direction in the dz^2 band (Figure S5J).

As for the Ag–Bi case, the axial effect will push the entire Ag dz^2 band up in energy relative to the Ag dx^2-y^2 band. The magnitude of the axial effect should be the same as in the Ag–Bi case, where the dz^2 band is pushed high enough to reach the same maximum as the dx^2-y^2 band (main text Figure 8H). However, in the Ag–Bi structure, strong antibonding interactions between Bi s and halide p orbitals at the B′ site generate the maximum of the dx^2-y^2 band (main text Figure 8F). Since we assume Tl d orbitals do not make significant contributions to the VB in the Ag–Tl $n = 1$ (see Section S5.3 for justification), weaker 90° X-X antibonding interactions set the maximum of the dx^2-y^2 band in this case (Figure S5F). Thus, we predict that the maximum energy reached by the dx^2-y^2 band in the Ag–Tl structure will be lower than in the Ag–Bi structure, meaning that the VBM will be formed by the dz^2 band at M (Figure S5J).

S5.1.2 Predictions for the conduction band

The root MO of the CB in 3D $Cs_2AgTlBr_6$ is the antibonding combination of the Tl 6s LUMO with the halide SALC of matching symmetry, so, to map out the CB of the $n = 1$ structure, we consider the $A_{1g}^{(s)}$-derived Bloch waves (main text Figure 6) which have s orbital symmetry at the B site. Given that Ag 5s orbitals contribute to the CBM of $Cs_2AgTlBr_6$, we expect they will also be involved in the CBM of the $n = 1$ structure. Thus, considering the Ag-X and 90° X-X interactions at the Ag site, we arrive at an energetic ranking of Γ < X < M for the Tl s-derived CB (Figure S5G-I), with Ag 5s contributions expected at the CBM at Γ. The predicted CB is shown as the purple line in Figure S5J.

S5.1.3 Comparison of predictions to DFT calculations

Comparing our predicted band structure to that computed by DFT (Figure S5K), we note good agreement between the patterns of band dispersion in both the valence and conduction bands. We also find that the maximum reached by the dz^2 band is 60 meV higher than that reached by the dx^2-y^2 band, in line with our prediction that the axial effect will dominate in this system. However, it is worth noting that, in contrast to our prediction, DFT shows no Ag s character at the Γ point. Nevertheless, the CBM remains at Γ since the in-phase arrangement of halide p orbitals at the B′ site contributes bonding character.

S5.2 The *n* = 2 Ag–Tl structure

S5.2.1 Predictions for the valence band

As for the $n = 1$ case, we derive the highest VBs of the Ag–Tl $n = 2$ structure from the Ag dz^2 and dx^2-y^2 orbitals and the CB from Tl s orbitals. The full LCAO representations of each band at the M, X, and Γ points are given in Figure S6. Note that all bands are doubly degenerate at the M and X points but the Ag dz^2 and Tl s bands split at Γ, and the two non-degenerate representations (arising from in-phase and out-of-phase combinations of the starting SALCs, see main text Section 2.4.2) are given in Figure S6. Based on these representations, we arrive at the predicted band diagram given in Figure S7.

Unlike in the n = 1 structure where the Ag dz^2 band generates the VBM at M, here we predict an Ag $dx^2–y^2$-based VBM at Γ because of the diminished axial effect. Considering only the interactions at the B′ site, the Ag $dx^2–y^2$ band at Γ (Figure S6G) is identical to its n = 1 analogue (Figure S5F). Similarly, the

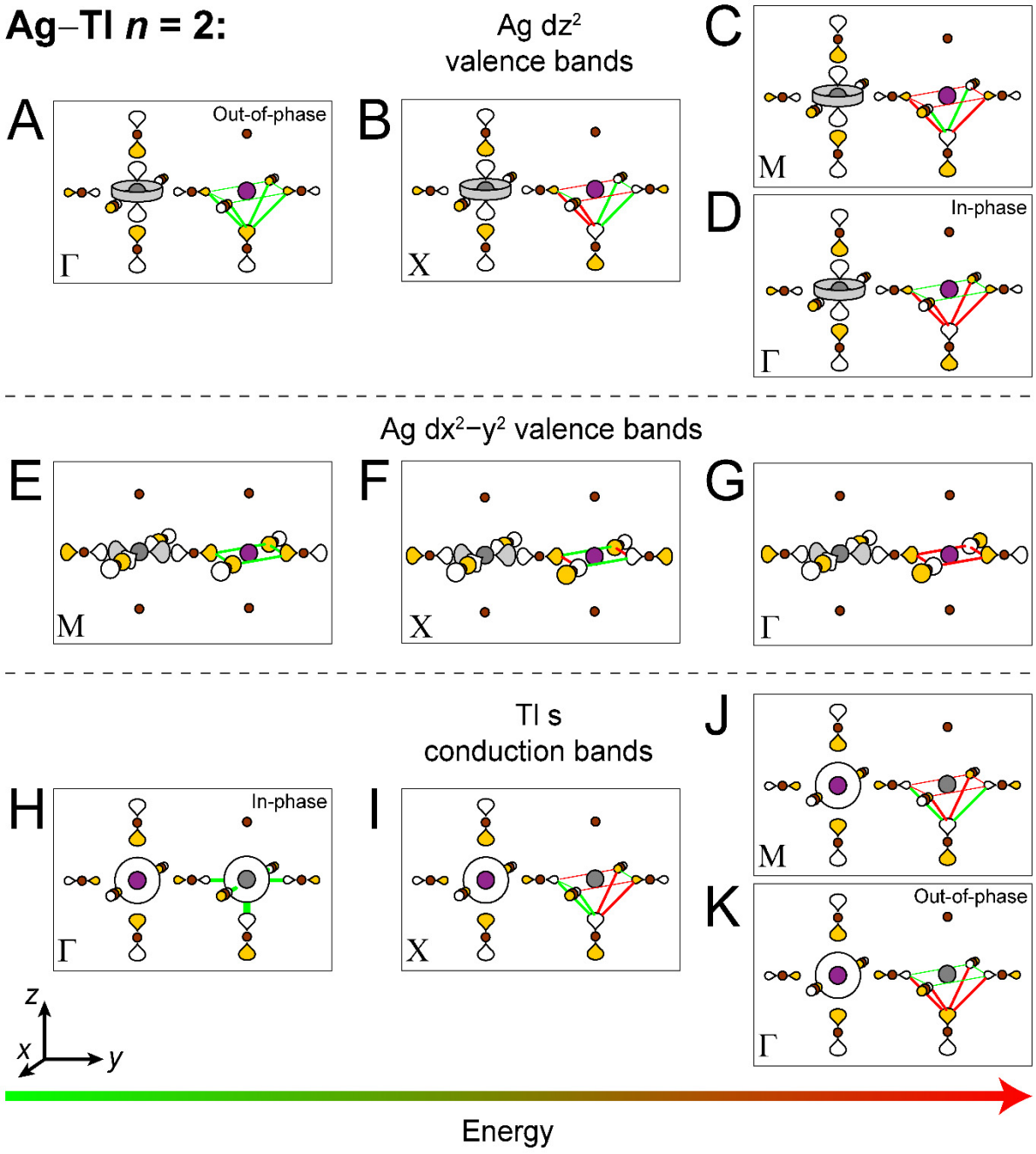

Figure S6. LCAO depictions of the Ag dz^2 (A-D), Ag $dx^2–y^2$ (E-G), and Tl s (H-K) bands of the Ag–Tl n = 2 structure at the M, X, and Γ points ranked in order of increasing energy from left to right. These depictions were used to derive the predicted band structure given in Figure S7. In cases where in-phase and out-of-phase starting SALC combinations give degenerate Bloch waves, we give only one depiction. The bonding and antibonding interactions at the B′ site are shown as green and red lines, respectively, and the thickness of each line corresponds to the strength of the interaction. Gray and purple spheres represent Ag and Tl atoms, respectively. Halide p orbital lobes are scaled to represent approximate relative electron densities.

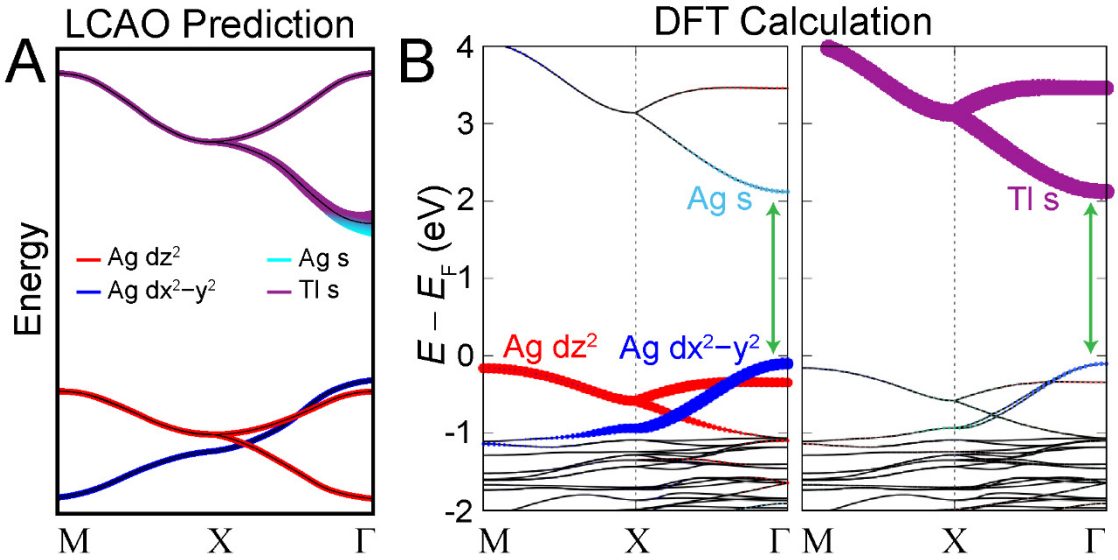

Figure S7. (A) Predicted band diagram of the n = 2 Ag–Tl structure derived using the LCAO representations given in Figure S6. (B) DFT band structure of the n = 2 Ag–Tl structure.

Ag dz^2 band at M (Figure S6C) is equivalent to its n = 1 analogue (Figure S5C) because the bridging axial halide p orbital present at the B′ site in the n = 2 case is non-bonding with respect to the four equatorial p orbitals and therefore, does not affect the energy of the Bloch wave. However, considering the B-site interactions, we expect the axial effect to be less pronounced than in the n = 1 structure because we have only one terminal halide in the n = 2 structure. This will lower the energy of the dz^2 band relative to its position in the n = 1, resulting in a dx^2–y^2-derived VBM at Γ. Note that it is difficult to assign the energy of the two degenerate dz^2 bands at M (Figure S6C) relative to that of the in-phase dz^2 band at Γ (Figure S6D). (This same difficulty arises in n = 2 Ag–Bi structure, see Figure S17B,C). Both are expected to have net antibonding 90° X-X interactions at the B′ site, but which is higher in energy depends on the strength of the 90° X-X interaction between two small equatorial halide p orbital lobes relative to the interaction between a small equatorial lobe and the large axial lobe. Such an analysis is beyond the scope of this work and furthermore, this subtle point does not affect any of the important aspects of the band structure. Thus, we assume that these two antibonding configurations are isoenergetic both here and in the Ag–Bi case (Figure S17B,C).

S5.2.2 Predictions for the conduction band

In the CB, we predict that the in-phase combination of the two $A_1^{(s)}$ SALCs will form the CBM at Γ with stabilizing contributions from Ag s orbitals. The band derived from the out-of-phase combination will follow the same pattern of dispersion from M to X but split off to higher energy at Γ as the 90° X-X interactions contribute antibonding character (Figure S6H-K and Figure S7A). For the same reasons described in the paragraph above, it is difficult to assign the energy of the out-of-phase Tl s band at Γ (Figure S6K) relative to that of both Tl s bands at M (Figure S6J), so we treat them as isoenergetic. As noted earlier (Section S5.2.1), this point does not affect the important aspects of the band structure.

S5.2.3 Comparison of predictions to DFT calculations

Once again, we find qualitatively good agreement between our predicted band structure and the one calculated using DFT (Figure S7B). Most notably, the DFT band structure shows a VBM at Γ that is 60 meV higher in energy than the top of the VB at M, confirming our assessment that the equatorial effect dominates over the axial effect in this structure. Thus, in both the Ag–Tl and Ag–Bi (see main text Section 2.5.3) systems, the equatorial effect becomes more important than the axial effect when we move from the $n = 1$ to the $n = 2$ structure.

S5.3 Contributions of Tl d orbitals to the VB

In the above case studies, we successfully predict the dispersion patterns of the Ag dz^2- and $dx^2–y^2$-based VBs under the assumption that the HOMOs of Tl (the dz^2 and $dx^2–y^2$ orbitals) do not make substantial contributions to these bands. However, it is worth pointing out that DFT predicts small amounts of Tl d character are, in fact, present in these bands in the 3D, $n = 2$, and $n = 1$ structures (Table S1). These contributions are similar in magnitude to the contributions of Bi s orbitals to the VB of the Ag–Bi structure (Table S1).

Note that these Tl d orbital contributions are not observed in the band structures predicted by DFT for Cs_2AgTlX_6 (X = Cl, Br) in our previous work.[5] This is due the use of different hybrid functionals and different computational methods to account for the anomalous bandgap predictions of DFT calculations for $Cs_2AgTlBr_6$. As reported before,[5] the use of the exchange-correlation functional of Perdew, Burke, and Ernzerhofer (PBE)[6] leads to a negative bandgap for $Cs_2AgTlBr_6$. The use of the PBEsol[7] functional also leads to the prediction of metallic character for $Cs_2AgTlBr_6$ (Section S2). The use of the screened hybrid functional of Heyd, Scuseria, and Ernzerhof (HSE06)[8] leads to a nonnegative bandgap, but still severely underestimates the experimentally observed bandgap. In our previous work, the bandgaps of Cs_2AgTlX_6 (X = Cl, Br) were calculated using Green's function-based many-body perturbation theory[9] calculations in a "one-shot" G_0W_0 framework[10, 11] using the HSE06 orbitals and eigenvalues as inputs. The DFT band structures of Cs_2AgTlX_6 were calculated with the HSE06 functional and the conduction bands were rigidly shifted so the bandgap matched the G_0W_0@HSE06 bandgap. In this work (Section S2), we instead used a 6×6×6 *k*-point grid and a modified version of the PBE0 functional with 35% of exact exchange for our band structure calculations of $Cs_2AgTlBr_6$ and the corresponding mono- and bilayer model structures. Apart from the presence of Tl d-orbital character composition in the 3D Ag–Tl band structure, the orbital compositions, and patterns of dispersion of the VBs and CB are consistent between the two different calculations.

The fact that we successfully predict the dispersion pattern of the Ag d-based VBs of the Ag–Tl systems while neglecting Tl d contributions can be explained by two factors. First, Tl $dx^2–y^2$ orbitals will contribute antibonding character to Bloch waves where the 90° X-X interactions at the B′ site are antibonding (for example, Figure S5C,F), thereby maintaining the antibonding character of the Bloch wave at the B′ site and not significantly changing the overall dispersion pattern of the band. Second, Tl 5d orbitals are much less diffuse than Bi 6s orbitals, so their antibonding interaction with the surrounding halide p orbitals will be weaker and have less influence on band dispersion. This is well demonstrated by two points. First, DFT shows that despite similar contributions of Bi s (8.8%) and Tl $dx^2–y^2$ (9.8%) orbitals to the Ag $dx^2–y^2$ bands of the $n = 1$ Ag–Bi and Ag–Tl structures (at M and Γ, respectively; Table S1), the Tl $dx^2–y^2$ orbitals contribute less antibonding character, evidenced by the fact that the VBM of the Ag $dx^2–y^2$ band is lower in energy than that of the Ag dz^2 band (Figure S5K) unlike in the Ag–Bi structure (main text Figure 8H). Second, the $n = 1$ Ag dz^2 and $dx^2–y^2$ bands remain bonding (lowest in energy) at Γ and M, respectively (Figure S5K), despite the small antibonding contributions from Tl dz^2 orbitals here (4.5% and 9.5% at Γ

and M, respectively). This indicates that the interactions between the Tl dz^2 orbitals and surrounding halide p orbitals are weaker than the 90° X-X interactions and can be neglected for the purposes of this work.

Table S1. Metal orbital composition of the VBM at the 3D X or 2D M point and at the Γ point for the 3D and 2D Ag–Bi, Ag–Sb, and Ag–Tl structures.

		VBM at X (3D) or M (2D)	VBM at Γ
Ag–Bi	3D	33.1% Ag dz^2, 10% Bi s	43.4% Ag $dz^2(dx^2-y^2)$*, 0% Bi s
	$n = 2$	32.2% Ag dx^2-y^2, 2.8% Ag dz^2, 9.8% Bi s	34.6% Ag dz^2, 6.6% Bi s
	$n = 1$	37% Ag dx^2-y^2, 8.8% Bi s	41.6% Ag dz^2, 3.1% Bi s
Ag–Sb	3D	29% Ag dz^2, 13.8 % Sb s	45% Ag $dz^2(dx^2-y^2)$*, 0% Sb s
	$n = 1$	30.8% Ag dx^2-y^2, 13.4% Sb s	38.5% Ag dz^2, 5.3% Sb s
Ag–Tl	3D	27.1% Ag dx^2-y^2, 10.1% Tl dx^2-y^2	27.1% Ag dz^2 (dx^2-y^2), 10.1% Tl dz^2 (dx^2-y^2)*
	$n = 2$	27% Ag dz^2, 2.7% Ag dx^2-y^2, 3.2% Tl dx^2-y^2, 2.8% Tl dz^2	28.6% Ag dx^2-y^2, 10% Tl dx^2-y^2
	$n = 1$	32.6% Ag dz^2, 3.8% Tl dx^2-y^2	30.4% Ag dx^2-y^2, 9.8% Tl dx^2-y^2

*The Ag dz^2 and Ag dx^2-y^2 bands are degenerate and the same % composition applies to both.

S6 Extending the LCAO analysis to π-bonding states

The LCAO analysis demonstrated in the main text considers only the case where the metal orbitals form σ interactions with the surrounding halide p orbitals that point directly towards the metal B and B′ sites. To understand the band structures of the Ag–Bi and Ag–Tl compositions, it is sufficient to consider only the σ-bonding states to derive the most important features of the band structures since the frontier metal orbitals of Ag^+, Bi^{3+}, and Tl^{3+} can form strong σ interactions with the surrounding halide p orbitals. However, for cases where one or both of the metal cations has dxy/dxz/dyz frontier orbitals it is important to consider the π-bonding states involving interactions with the halide p orbitals that are orthogonal to the metal B and B′ sites.[12] While a full analysis of the π-bonding states is beyond the scope of this work, in the sections below, we include an analysis of the π-bonding states relevant to the derivation of bands based on the metal dxy/dxz/dyz orbitals. We do so to demonstrate that the factors described in the main text that affect the dispersion pattern and relative energies of the dz^2 and dx^2-y^2 bands (the axial effect, the equatorial effect, and 2D translational symmetry) are also important considerations for the dxy/dxz/dyz bands. This allows us to draw the more general conclusion stated in the main text that double perovskite compositions where either the VBM or CBM stems from a band based on any B-site metal d orbital are likely to undergo changes in the symmetry of the band extrema upon dimensional reduction. We also include an analysis of one additional π-bonding state that becomes important in the case where no metal orbitals contribute to the top

of the VB. Note that we still describe this state as "π-bonding" despite the absence of metal orbital contributions because it involves the same halide p orbitals that are orthogonal to the B and B′ sites.

S6.1 Derivation of selected π-bonding SALCs and Bloch waves for the $n = 1$ case

We construct π-bonding SALCs for the $[BX_6]^{n-}$ root MO of an $n = 1$ structure by considering the π-bonding p orbitals on the six halide atoms surrounding the B site. As for the σ-bonding case, we operate according to D_{4h} point symmetry. Labels for the twelve π-bonding halide p orbitals are defined in Figure S8A and the different colors of the orbital lobes denote symmetry equivalent halide orbitals. We generate three reducible representations ($\Gamma_{1\text{-}4}$, $\Gamma_{5\text{-}8}$, and $\Gamma_{9\text{-}12}$, Figure S8B), one for each set of symmetry related p orbitals, by tracking how many orbitals in each set are unaltered by each symmetry operation. By consulting the D_{4h} character table, we decompose $\Gamma_{1\text{-}4}$, $\Gamma_{5\text{-}8}$, and $\Gamma_{9\text{-}12}$ into irreducible representations, finding that $\Gamma_{1\text{-}4} \rightarrow A_{2u} + B_{2u} + E_g$, $\Gamma_{5\text{-}8} \rightarrow A_{2g} + B_{2g} + E_u$, and $\Gamma_{9\text{-}12} \rightarrow E_g + E_u$. According to the D_{4h} character table, the metal dxy orbital has B_{2g} symmetry while the metal dxz and dyz orbitals have E_g symmetry. Thus, to understand the bands derived from these metal d orbitals, we only need to consider the B_{2g} and E_g SALCs.

We construct and normalize halide SALCs of B_{2g} and E_g symmetry by applying the method of projection operators described in Section S3.1. Projection tables for one p orbital from each symmetry-related set are given in Figure S8C. For the SALC of B_{2g} symmetry, we find:

$$\boldsymbol{B_{2g}}: \boldsymbol{P_{B_{2g}}}(\varphi_5) = \frac{1}{2}(\varphi_5 - \varphi_6 + \varphi_7 - \varphi_8)$$

We find four SALCs of E_g symmetry, each involving only two halide p orbitals:

A

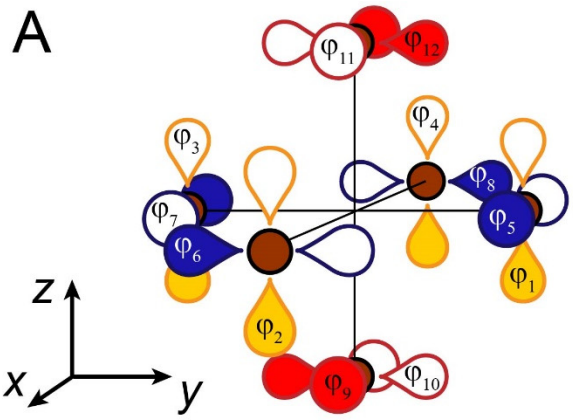

B

D_{4h}	E	$2C_4(z)$	C_2	$2C_2'$	$2C_2''$	i	$2S_4$	σ_h	$2\sigma_v$	$2\sigma_d$	$\Gamma_{irreducible}$
$\Gamma_{1\text{-}4}$	4	0	0	-2	0	0	0	-4	2	0	$A_{2u} + B_{2u} + E_g$
$\Gamma_{5\text{-}8}$	4	0	0	-2	0	0	0	4	-2	0	$A_{2g} + B_{2g} + E_u$
$\Gamma_{9\text{-}12}$	4	0	-4	0	0	0	0	0	0	0	$E_g + E_u$

C

Starting orbital:	E	$2C_4(z)$	C_2	$2C_2'$	$2C_2''$	i	$2S_4$	σ_h	$2\sigma_v$	$2\sigma_d$
φ_1	φ_1	φ_2, φ_4	φ_3	$-\varphi_1$, $-\varphi_3$	$-\varphi_2$, $-\varphi_4$	$-\varphi_3$	$-\varphi_2$, $-\varphi_4$	$-\varphi_1$	φ_1, φ_3	φ_2, φ_4
φ_5	φ_5	φ_6, φ_8	φ_7	$-\varphi_5$, $-\varphi_7$	$-\varphi_6$, $-\varphi_8$	φ_7	φ_6, φ_8	φ_5	$-\varphi_5$, $-\varphi_7$	$-\varphi_6$, $-\varphi_8$
φ_9	φ_9	φ_{10}, $-\varphi_{10}$	$-\varphi_9$	φ_{11}, $-\varphi_{11}$	φ_{12}, $-\varphi_{12}$	φ_{11}	φ_{12}, $-\varphi_{12}$	$-\varphi_{11}$	φ_9, $-\varphi_9$	φ_{10}, $-\varphi_{10}$

Figure S8. Derivation of π-bonding SALCs for the undistorted $n = 1$ structure. (A) The D_{4h}-symmetric arrangement of the twelve π -bonding halide p orbitals around the B site. Sets of symmetry related orbitals are drawn in the same color. (B) Reducible representations for the three sets of symmetry-related p orbitals and their decomposition into irreducible representations. (C) Projection table for the φ_1 and φ_5 and φ_9 orbitals.

$$\boldsymbol{P}_{E_g}(\varphi_1) = \frac{1}{\sqrt{2}}(\varphi_1 - \varphi_3)$$

$$\boldsymbol{P}_{E_g}(\varphi_2) = \frac{1}{\sqrt{2}}(\varphi_2 - \varphi_4)$$

$$\boldsymbol{P}_{E_g}(\varphi_9) = \frac{1}{\sqrt{2}}(\varphi_9 + \varphi_{11})$$

$$\boldsymbol{P}_{E_g}(\varphi_{10}) = \frac{1}{\sqrt{2}}(\varphi_{10} + \varphi_{12})$$

Taking linear combinations of the first and fourth SALCs and of the second and third SALCs yields new SALCs involving four halide p orbitals that have the correct symmetry to interact with the metal dyz and dxz orbitals, respectively:

$$\boldsymbol{E_g^{(1)}}: \frac{1}{\sqrt{2}}\boldsymbol{P}_{E_g}(\varphi_1) - \frac{1}{\sqrt{2}}\boldsymbol{P}_{E_g}(\varphi_{10}) = \frac{1}{2}(\varphi_1 - \varphi_3 - \varphi_{10} - \varphi_{12})$$

$$\boldsymbol{E_g^{(2)}}: \frac{1}{\sqrt{2}}\boldsymbol{P}_{E_g}(\varphi_2) + \frac{1}{\sqrt{2}}\boldsymbol{P}_{E_g}(\varphi_9) = \frac{1}{2}(\varphi_2 - \varphi_4 + \varphi_9 + \varphi_{11})$$

These B_{2g} and E_g SALCs (shown in Figure S9) are propagated across the n = 1 lattice (as demonstrated for the σ-bonding halide SALCs in main text Figure 5) according to the translational symmetry rules of the Γ, X, and M points, thus generating the halide Bloch waves summarized in Figure S10.

S6.2 The axial and equatorial effects for dxy, dxz, and dyz bands

In main text Section 2.2.6, we described how the axial effect shifts the relative energies of the dz^2- and dx^2–y^2-based bands. This same effect also applies to bands based on metal dxz/dyz/dxy orbitals. In a perfectly octahedral ligand field with six equivalent metal-halide interactions, the metal dxz, dyz, and dxy orbitals are isoenergetic. However, as described in main text Section 2.2.6, the axial halide p orbitals of the n = 1 material are able to interact more strongly with a B-site metal orbital than the bridging halides because they are not shared between two metal centers. As a result, the bands derived from metal dxz and dyz orbitals (which interact with the axial halide p orbitals) will be shifted up in energy relative to the band derived from the metal dxy orbital (which interacts only with the equatorial halide p orbitals).

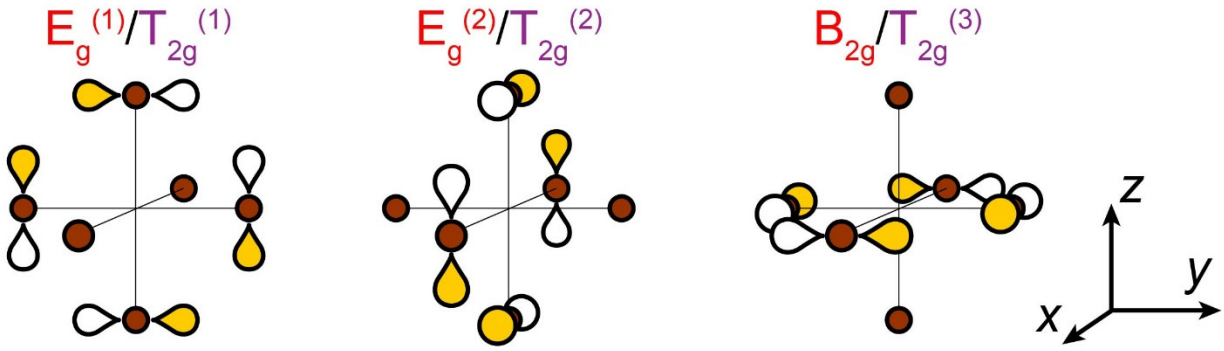

Figure S9. The three n = 1 π-bonding halide SALCs, which have the appropriate symmetry to interact with metal dyz ($E_g^{(1)}$), dxz ($E_g^{(2)}$), dxy (B_{2g}) orbitals. These SALCs are completely analogous to the three T_{2g} SALCs of the 3D lattice (symmetry labels shown in purple).

The equatorial effect, described in main text Section 2.2.5 in the context of the dz^2- and $dx^2{-}y^2$-based bands, also comes into play for bands based on metal dxz/dyz/dxy orbitals. The E_g SALCs (which form the basis for the dyz/dxz bands, Figure S9) involve the axial halide p orbitals, which are not propagated to the B′ site by translational symmetry (main text Section 2.2.2 and Figure S10). Thus, relative to the Bloch waves derived from the B_{2g} starting SALC (which involves only the equatorial halide p orbitals and forms the basis for the dxy band, Figure S9) the E_g-derived Bloch waves will form weaker bonding/antibonding interactions at the B′ site because of the diminished halide p-orbital participation (Figure S10). As for the $dz^2/dx^2{-}y^2$ case, the axial and equatorial effects will compete to determine the location and orbital composition of the VBM in cases involving filled dxz/dyz/dxy frontier orbitals: the axial effect will raise the energy of the dyz/xz-based VBM while the equatorial effect will raise the energy of the dxy-based VBM.

S6.3 3D vs 2D translational symmetry: effects on the dxy, dxz, and dyz bands

In main text Section 3.1 and in Section S8 below, we describe how the shift from 3D to 2D translational symmetry leaves the dispersion pattern of bands based only on metal s and p orbitals unaffected but alters the dispersion pattern of bands with metal dz^2 and $dx^2{-}y^2$ character. We trace this change in dispersion pattern to the differences in metal dz^2- and $dx^2{-}y^2$-orbital interactions found in the *xy* and *yz*/*xz* planes. Here we extend these arguments to bands based on metal dyz/dxz/dxy orbitals to show that the shift to 2D translational symmetry can also change the pattern of band dispersion for bands derived from these metal d orbitals.

The $n = 1$ E_g and B_{2g} SALCs are directly analogous to the three T_{2g} SALCs derived for the 3D case (Figure S9) so for simplicity, in the text below, we refer to these SALCs according to their 3D $T_{2g}^{(1,2,3)}$ labels as we compare the 3D and 2D Bloch waves derived from each one. Importantly, in the T_{2g} SALCs the halide

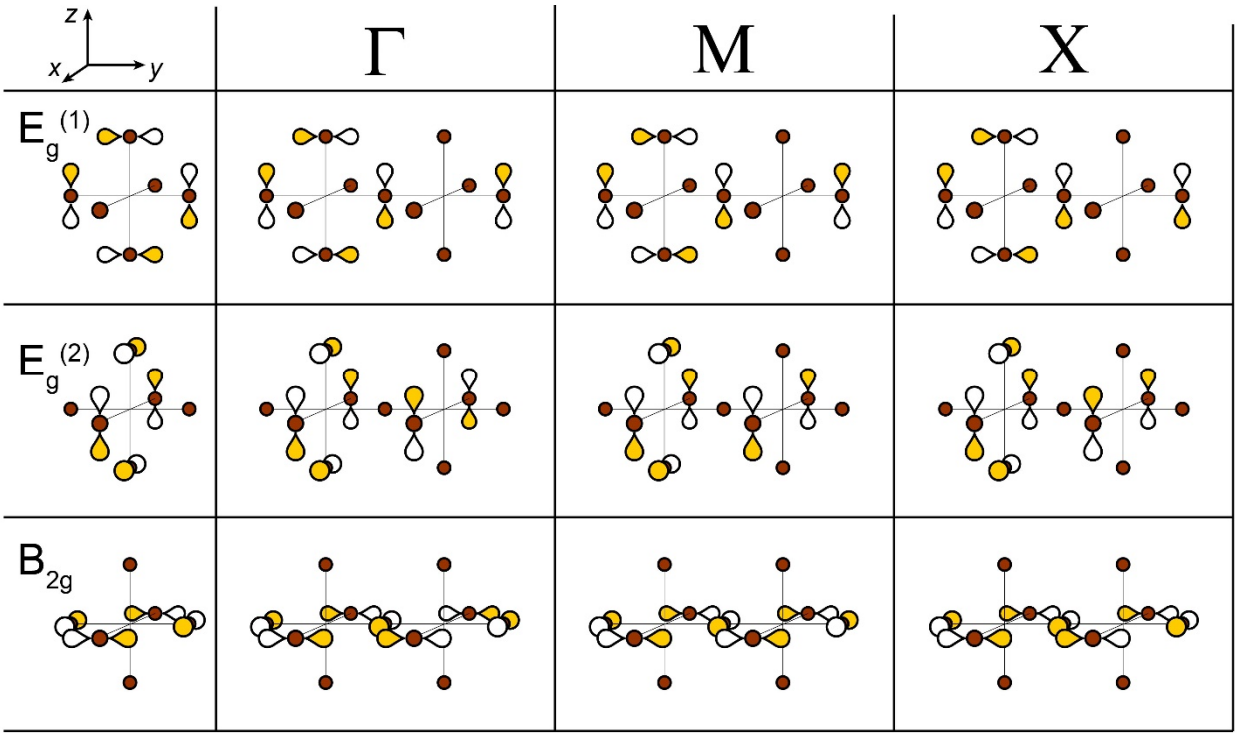

Figure S10. A summary of the $n = 1$ halide Bloch waves generated from the $E_g^{(1,2)}$ and B_{2g} starting SALCs at the high-symmetry Γ, M, and X points.

orbital environments in the *xy* and *yz* planes are not equivalent. For example, in the $T_{2g}^{(3)}$ SALC, there are four halide p orbitals and four bonding 90° halide-halide interactions in the *xy* plane, while in the *yz* plane, there are only two halide p orbitals and no 90° halide-halide interactions. In the main text, we demonstrated how differences between the halide p-orbital environments in the *xy* and *yz* planes of the 3D $E_g^{(1,2)}$ SALCs (which interact with metal dz^2 and dx^2-y^2 orbitals) lead to a different pattern of dispersion for the $E_g^{(1,2)}$-derived bands in the 3D and 2D cases. Below, we give several examples to demonstrate how this same effect applies to the T_{2g} SALCs resulting in different patterns of dispersion for the 3D and 2D dyz/dxz/dxy-based bands.

S6.3.1 Example 1: The dxy band

Unlike for the 3D A_{1g} and T_{1u} SALCs, translations along the *xy* and *yz* plane are not equivalent for the $T_{2g}^{(3)}$ SALC (from which the dxy band is derived). Antisymmetric translation of the $T_{2g}^{(3)}$ SALC in the *yz* plane (at the 3D X point) produces a Bloch wave with the appropriate symmetry to form antibonding interactions with a dxy orbital of the B′ metal (Figure S11A), but when this antisymmetric translation moves to the *xy* plane in the 2D lattice (at the M point), the halide environment at the B′ site no longer has the right symmetry to interact with a dxy metal orbital at the B′ site (Figure S11B). Note that the 90° X-X interactions formed in the 3D and 2D halide Bloch waves also differ between the 3D and 2D case here. Thus, we expect the dispersion pattern of the $T_{2g}^{(3)}$-derived (dxy) band to change moving from the 3D to the 2D perovskite lattice. This is analogous to the case of the $E_g^{(2)}$-derived band presented in main text Section 3.1.3.

S6.3.2 Example 2: The dyz/dxz bands

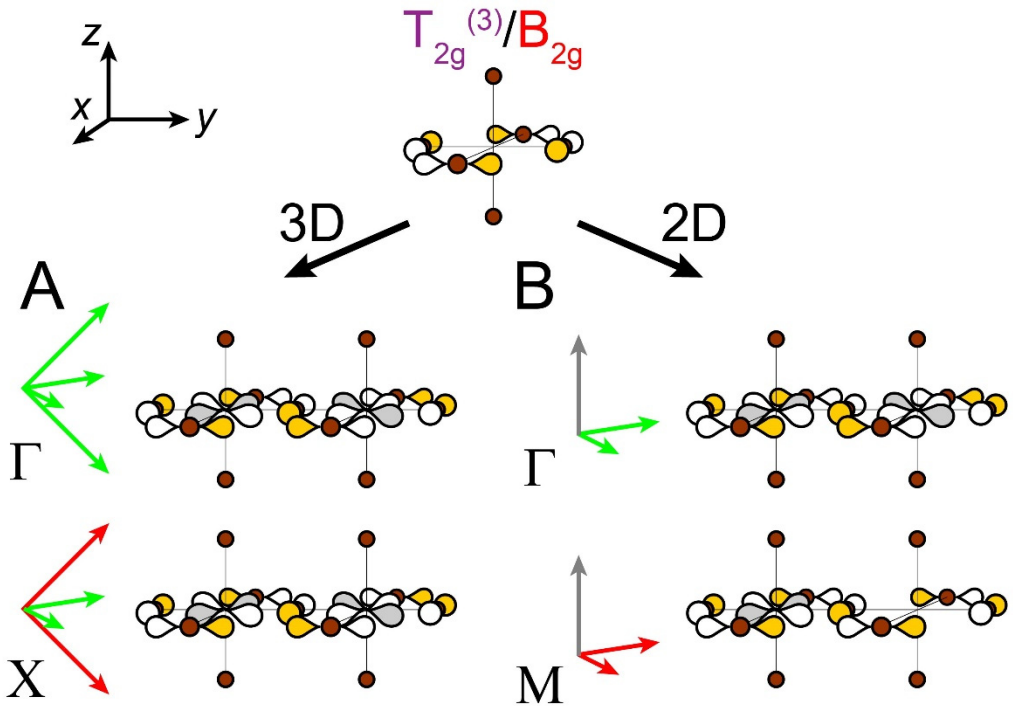

Figure S11. Halide Bloch waves derived from the 3D $T_{2g}^{(3)}$ SALC (analogous to the 2D B_{2g} SALC) according to the translational symmetry rules of the 3D (A) and 2D (B) perovskite lattices. In cases where the halide p orbital environment has the appropriate symmetry to interact with a B- or B′- site metal orbital, these orbitals are shown to highlight how 3D and 2D translational symmetry is expected to generate distinct patterns of band dispersion.

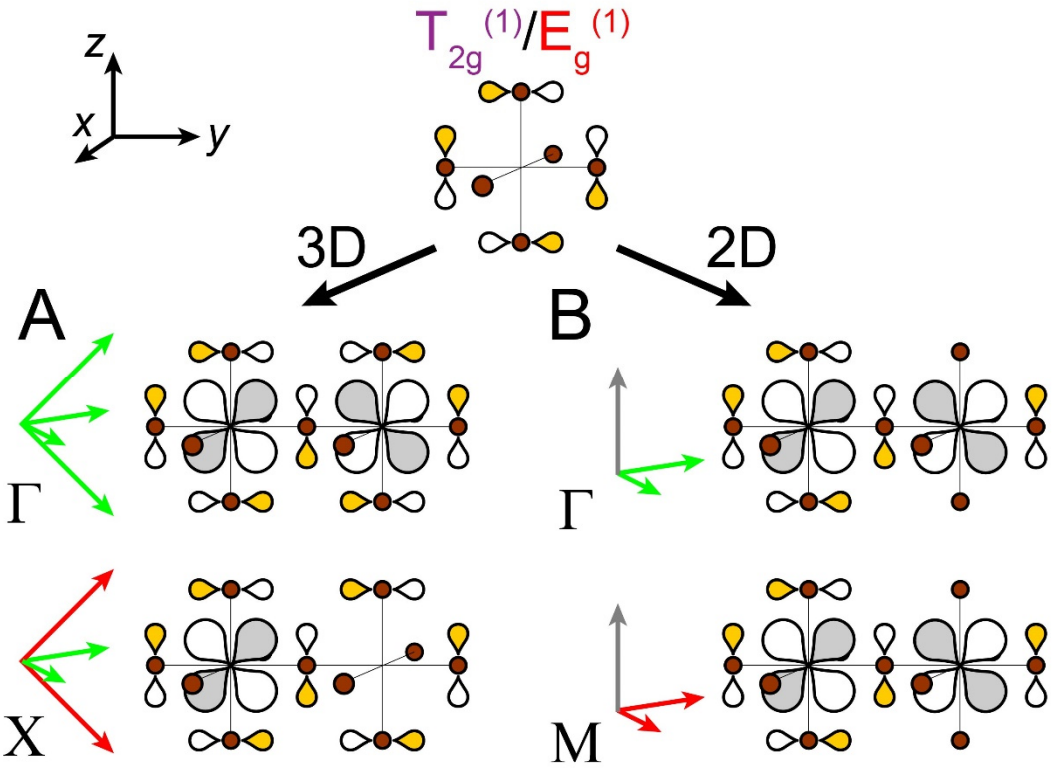

Figure S12. Halide Bloch waves derived from the 3D $T_{2g}^{(1)}$ SALC (analogous to the 2D $E_g^{(1)}$ SALC) according to the translational symmetry rules of the 3D (A) and 2D (B) perovskite lattices. In cases where the halide p orbital environment has the appropriate symmetry to interact with a B- or B′- site metal orbital, these orbitals are shown to highlight how 3D and 2D translational symmetry is expected to generate distinct patterns of band dispersion.

In both the 2D and 3D case, symmetric translation of the $T_{2g}^{(1)}$ SALC at the Γ point generates a halide environment at the B′ site with the proper symmetry to interact with a B′ metal dyz orbital (Figure S12). The antisymmetric translation in the *yz* plane at the 3D X point flips the phase of the axial p orbitals at the B′ site, generating a halide environment that *cannot* interact with a B′ metal dyz orbital (Figure S12A). However, in the 2D case, this antisymmetric translation moves to the *xy* plane, maintaining a halide p orbital environment that can interact with a dyz orbital of the B′ metal (Figure S12B). Thus, the dispersion pattern of the $T_{2g}^{(1)}$-derived (dyz) band is expected to change moving from the 3D to the 2D perovskite lattice. Similar arguments apply to the $T_{2g}^{(2)}$-derived (dxz) band. Note that for simplicity and ease of visualization, here we treat the three 3D π-bonding T_{2g} states (and the two 2D π-bonding E_g states) separately, but similar to the three 3D σ-bonding T_{1u} states (and the two 2D σ-bonding E_u states), we can take linear combinations of these symmetry-matching states as described in Sections S6.1 and S6.2 above. However, since these T_{2g} states are not capable of interacting with one another (i.e. the halide p orbitals of the $T_{2g}^{(1)}$ SALC cannot form 90° X-X interactions with those of the $T_{2g}^{(2)}$ or $T_{2g}^{(3)}$ SALCs) an analysis of these linear combinations would yield the same conclusion.

S6.4 A note of caution in analyzing π-bonding states in the 2D case

The analysis presented above allows us to expand the arguments made in the main text for bands with dz^2 and $dx^2–y^2$ metal orbital character to include bands with dyz/dxz/dxy metal orbital character and to make the more general statement that double perovskite compositions where either the VBM or CBM is from a

band based on any B-site metal d orbital, are likely to undergo changes in the symmetry of the band extrema upon dimensional reduction. However, it is important to caution the reader that an in-depth analysis of the π-bonding states using the method presented here will not be as worthwhile or accurate as for the σ-bonding states. In the 3D case, inspection of band structures where dyz/dxz/dxy orbitals contribute to the band edges shows that these bands are generally relatively flat compared to bands based on metal s, p, or $dz^2/dx^2–y^2$ orbitals.[13] This is expected since B-X π-bonds are relatively weak in comparison to B-X σ-bonds, generating bands with less dispersion. These π-based bands will become even flatter in the 2D case as dimensional reduction leads to a further reduction in dispersion. Not only does it become less meaningful to predict the band extrema in cases where bands are very flat (because the differences between the smallest direct and indirect gaps becomes very small) but also, it becomes increasingly hard to accurately predict the band extrema because subtle factors not easily accounted for using our simple method (such as orbital mixing or unexpected orbital contributions) can cause slight alterations in dispersion, which become increasingly important in determining the band extrema of flat bands.

S6.5 The A_{2g}-derived band

There is one additional π-bonding band that is relevant to highlight: the band based on the A_{2g} SALC (Figure S13). This SALC is constructed from the four in-plane equatorial halide p orbitals (orbitals 5-8 in Figure S8A) with relative phases distinct from those found in the π-bonding B_{2g} SALC (Figure S9) and defined by the projection operator as:

$$\boldsymbol{A_{2g}}\boldsymbol{:}\, \boldsymbol{P_{A_{2g}}}(\varphi_5) = \frac{1}{2}(\varphi_5 + \varphi_6 + \varphi_7 + \varphi_8)$$

Note that the A_{2g} SALC is completely analogous to the 3D π-bonding $T_{1g}^{(3)}$ SALC. Figure S13 depicts the A_{2g}-derived Bloch waves at the Γ, X, and M points. Importantly, these Bloch waves bear a striking resemblance to those derived from the σ-bonding B_{1g} SALC (main text Figure 6): at each *k*-point, both sets have the same number of bonding and antibonding 90° X-X interactions. While the positioning within the lattice of these 90° X-X interactions differs between the two Bloch waves (centered around the metal center in the B_{1g} case and around the space between metal centers in the A_{2g} case), in the absence of metal orbital contributions to the VB, this difference does not matter because the dispersion pattern of the band is determined by the 90° X-X interactions alone. Therefore, in the absence of metal-orbital contributions to the VBM, the A_{2g}-derived band will compete with the $A_{1g}^{(d)}$- and B_{1g}-derived bands to form the VBM (see Section S9).

S7 Analogy between 3D and 2D halide SALCs and splitting of the 3D T_{1u} SALCs at the X point and in the 2D case

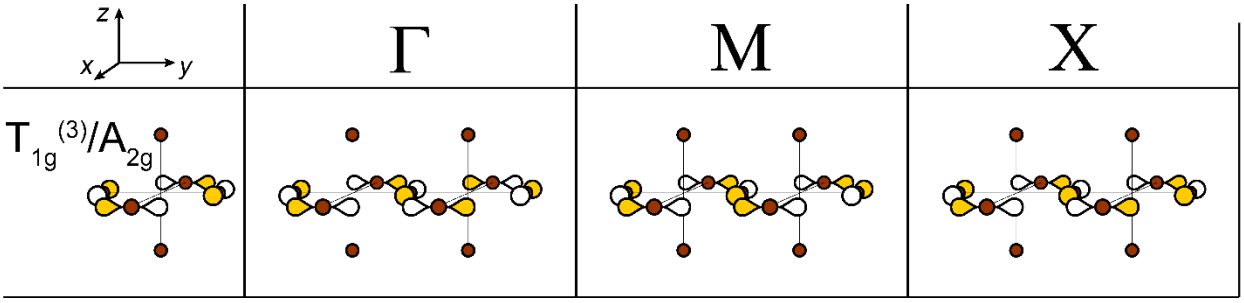

Figure S13. The $n = 1$ A_{2g} halide SALC and the halide Bloch waves derived from this SALC at the high-symmetry Γ, M, and X points. Note that this SALC is analogous to the 3D $T_{1g}^{(3)}$ SALC.

In main text Section 3.1, we show that when the 3D A_{1g} and T_{1u} SALCs are translated according to 3D or 2D translational symmetry, we get bands with the same predicted pattern of dispersion, but when the 3D E_g SALCs are translated according to 3D or 2D translational symmetry, we get bands with different patterns of dispersion. To minimize the number of different symmetry labels used, we refer only to the 3D SALCs to make these arguments (i.e., instead of translating the 3D SALC according to the 3D translational symmetry rules and the analogous 2D SALC according to the 2D translational symmetry rules and then comparing the results, we translate only the 3D SALC according to both the 3D and 2D translational symmetry rules and compare the results).

The 3D A_{1g}, $E_g^{(1)}$, and $E_g^{(2)}$ SALCs are identical to the $n = 1$ $A_{1g}^{(s)}$, $A_{1g}^{(d)}$, and B_{1g} SALCs, respectively, so here, no justification of the decision to refer only to the 3D SALCs is required. However, the case of the three degenerate 3D T_{1u} SALCs requires slightly more justification because these have no exact $n = 1$ analogues since the T_{1u} set is split under D_{4h} symmetry into E_u and A_{2u} SALCs, neither of which is identical to the T_{1u} SALCs. The $E_u^{(2)}$ SALC is analogous to the T_{1u} SALC considered in main text Figure 11 but without the axial halide p orbitals. However, it is important to recognize that the axial halide p orbitals of this T_{1u} SALC do not play an important role in determining band dispersion when this SALC is propagated according to 2D translational symmetry because (i) the p orbital environment along the axial (z) direction is identical to those along the two equatorial (x and y) directions and (ii) these axial halides are not generated at the B′ site by translational symmetry anyway. Thus, we get the same result whether we propagate the 3D T_{1u} SALC or the 2D $E_u^{(2)}$ SALC across the 2D lattice, thereby justifying our decision to use only the T_{1u} SALC in main text Section 3.1 for simplicity. It is also important to point out that these same arguments apply to the 2D $E_u^{(1)}$ SALC and another of the three degenerate 3D T_{1u} SALCs not considered here. The 2D A_{2u} SALC, however, has no 3D analogue (except at the 3D X point, see below), but this SALC generates a dispersionless band, which does not have any consequences for the band extrema or the symmetry of the band-edge transition of the 2D lattices.

At the 3D X point, the three degenerate 3D T_{1u} SALCs split into a doubly degenerate pair of SALCs consisting of the halide p orbitals in the xy plane and a singly degenerate SALC consisting of the two halide p orbitals along the z axis.[12] The translational symmetry of the X point lowers the symmetry of SALCs from the initial point group O_h to the subgroup D_{4h}. This is a specific case of a general rule that occurs at all k-points other than the Γ point. However, because in other cases the SALCs are completely analogous regardless of this descent in symmetry (as discussed below for the T_{1u} SALCs for the L point), we omit these symmetry labels in other cases for clarity. A more in-depth theoretical discussion is beyond the scope of this work, but we refer the interested reader to the work of Dresselhaus, Dresselhaus, and Jorio.[14] Here, we show that this symmetry lowering does not affect the conclusions discussed in the main text. At the 3D X point, the symmetry is lowered from O_h to D_{4h}, and the 3D T_{1u} SALCs undergo a descent in symmetry to $E_u + A_{2u}$. Note that these T_{1u}-derived SALCs in D_{4h} are completely analogous to the 2D $E_u^{(1,2)}$ and A_{2u} SALCs. Unlike the three degenerate 3D T_{1u} SALCs, these do not have the same halide orbital environments in the xy and yz planes, the key criteria given in the main text as a determinant of whether a SALC will generate Bloch waves with the same pattern of dispersion in the 3D and 2D cases. However, the $E_u^{(1,2)}$ and A_{2u} SALCs are exceptions to this criteria, where this matching halide orbital environment does not matter because they give Bloch waves with equivalent halide p orbital environments at the B′ site for the case of both fully symmetric and fully antisymmetric translation along all axes. Thus, in the 3D case, when we have antisymmetric translation in the yz plane and symmetric translation in the xy plane at the X point, we get equivalent Bloch waves to those we get for the 2D case M point (equivalent to the X point in the 3D case) where antisymmetric translation occurs along the xy plane (Figure S21). A similar descent in

symmetry occurs at the L point where the symmetry is lowered from O_h to D_{3d} and the 3D T_{1u} SALCs undergo a descent in symmetry to E_u + A_{2u}. However, because the symmetry operations are different between D_{3d} and D_{4h}, the $E_u + A_{2u}$ SALCs in the D_{3d} point group are analogous to the 3D T_{1u} SALCs. Despite this descent in symmetry, the SALCs still generate equivalent Bloch waves at the 3D L point and the 2D X point (Figure S21). Note that while descent in symmetry also applies to other 3D halide SALCs at the X and L points, it does not affect our conclusions and we chose to omit it for simplicity and clarity.

S8 A note on d orbital contributions from the B′ cation

For the reasons described in main text Section 3.1, dimensional reduction is generally not expected to alter the dispersion pattern of bands derived from metal s or p orbitals. However, if dz^2 orbitals of the B′-site cation contribute to these bands, their dispersion patterns may change in the 2D materials. This is because 2D translational symmetry does not generate axial halide p orbitals at the B′ sites of the 2D lattice (main text Section 2.2.2) making it possible for a metal dz^2 orbital to participate in a Bloch wave with A_{1g} symmetry at the B′ site (four in-phase equatorial halides). In contrast, a metal dz^2 orbital cannot contribute to the analogous 3D Bloch wave with A_{1g} symmetry at the B′ site which has six in-phase halide p orbitals at the B′ site (Figure S14). Fundamentally, this difference is caused by the fact that the dz^2 orbital forms interactions in the *yz* plane that are not equivalent to (i.e., they are not the same phase as) those in the *xy* plane. Thus, when translational symmetry in the *yz* plane is lost in the 2D lattice, the dispersion pattern of bands with metal dz^2 contributions is expected to change. Note that the same is not true for metal $dx^2–y^2$ orbital contributions at the B′ site: since the $dx^2–y^2$ orbital does not have interactions along the *z*-direction, the loss of the axial halide p orbitals at the B′ site does not make it possible for this d orbital to symmetry-match with any B′-site halide orbital environments in the 2D lattice that it otherwise would not have been able to in the 3D case.

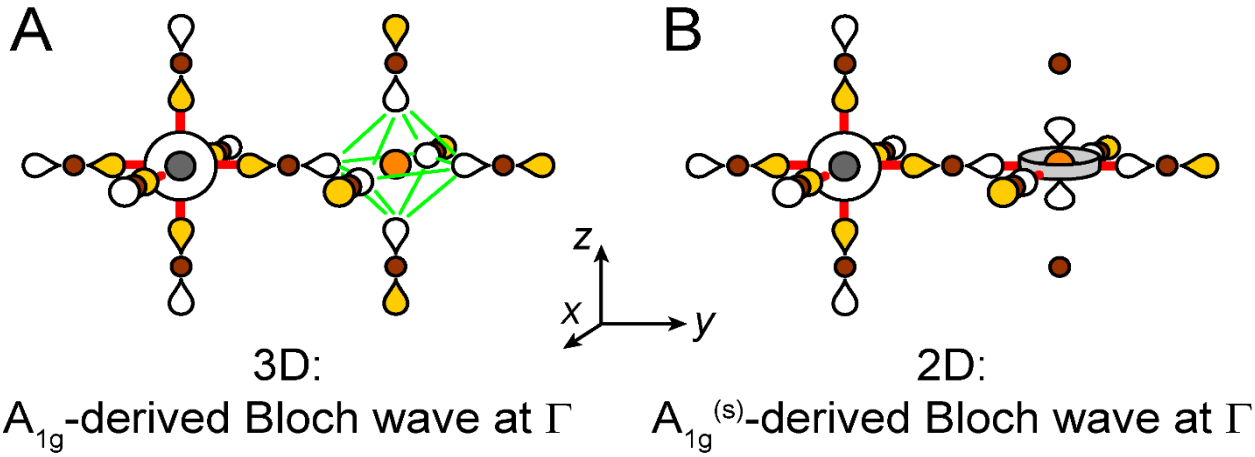

Figure S14. At Γ, 3D translational symmetry generates an A_{1g}-derived Bloch wave with six in-phase halide p orbitals at the B′ site where the 90° X-X interactions are all bonding (A). The analogous 2D $A_{1g}^{(s)}$-derived Bloch wave also has an in-phase configuration around the B′ site at Γ, but here, only the equatorial halides are involved (B, see main text Section 2.2.2). As a result, a dz^2 orbital of the B′ cation can participate in the 2D case but not in the 3D case. Therefore, for a VB derived from B-site metal s orbitals and B′-site metal dz^2/$dx^2–y^2$ orbitals, the Γ point will be the minimum in the 3D case but the maximum in the 2D case where the B′ dz^2 orbital introduces antibonding character. Gray and orange circles represent B and B′ cations, respectively.

S9 Bands with no metal orbital participation

In the main text, we consider only cases where at least one of the metal cations contributes a metal orbital to the valence and conduction bands. However, as discussed in our previous work,[12] it is also possible to have a VB where neither metal cation contributes and the band is composed solely of halide p orbitals. In this case, the highest VBs will be defined by the $A_{1g}^{(d)}$-, B_{1g}-, and A_{2g}-derived Bloch waves (in the n = 1 case, or the $A_1^{(d)}$-, B_1-, and A_2-derived Bloch waves in the n = 2 case) because these have the most antibonding 90° X-X interactions at the B site. The maximum of each of these bands will occur at the k-point where the 90° X-X interactions at the B′ site are also antibonding (the M point for the $A_{1g}^{(d)}$-derived band and the Γ point for the B_{1g}- and A_{2g}-derived bands). For the reasons discussed in main text Section 3.1, the dispersion patterns of the $A_{1g}^{(d)}$- and B_{1g}-derived bands will differ from their 3D analogues (derived from the analogous 3D $E_g^{(1)}$ and $E_g^{(2)}$ SALCs). Due to the analogy between the A_{2g}- and B_{1g}-derived Bloch waves discussed in Section S6.5, these same arguments also apply to the A_{2g}-derived band and its 3D counterpart, the $T_{1g}^{(3)}$-derived band. Thus, our model predicts that for double perovskite compositions where no metal orbitals contribute to the VB, dimensional reduction may lead to changes in the symmetry of the VBM. An analysis of which of these three competing bands will form the VBM in these cases is beyond the scope of this work, particularly since VBs formed without metal-orbital contributions are relatively flat.

S10 Additional Figures

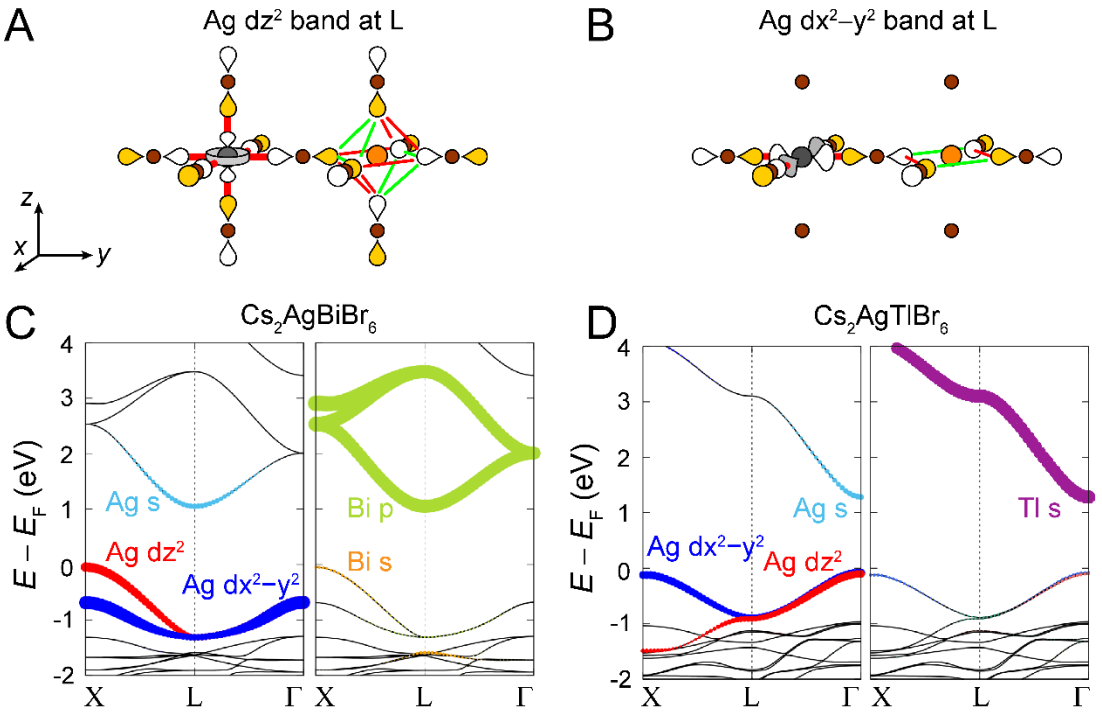

Figure S15. LCAO representation of the Ag dz^2 (A) and Ag dx^2–y^2 (B) bands at the L point for 3D $Cs_2AgBiBr_6$ and $Cs_2AgTlBr_6$. The bands are expected to be isoenergetic at the L point because the Ag dz^2 and dx^2–y^2 orbitals form equally strong antibonding interactions with the surrounding halide p orbital environments and the 90° X-X interactions around the Bi/Tl site are non-bonding. Band structures of $Cs_2AgBiBr_6$ (C, calculated without SOC) and $Cs_2AgTlBr_6$ (D) demonstrate that the two Ag d-based VBs are, in fact, isoenergetic at the L point. Gray and orange spheres represent Ag and Bi/Tl atoms, respectively.

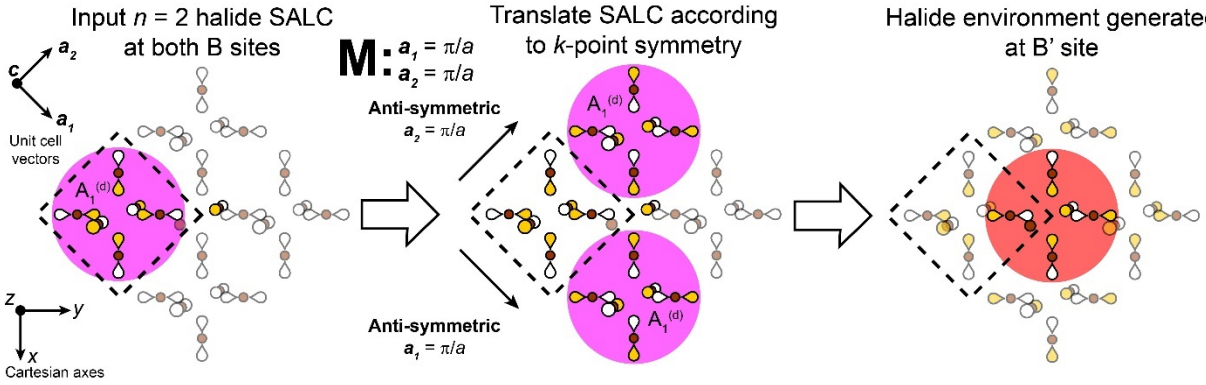

Figure S16. Example of the procedure for generating a halide Bloch wave for the $n = 2$ perovskite lattice. Here, we consider a top-down view of the perovskite lattice in which only the top layer of the $n = 2$ sheet is shown for clarity. We begin by placing $A_1^{(d)}$ SALCs around the two unique B sites of the $n = 2$ structure (one in the top layer, one in the bottom layer). Here, we show the in-phase combination of these SALCs. We then carry out antisymmetric translations of these SALCs along two in-plane unit cell vectors ($\boldsymbol{a_1}$ and $\boldsymbol{a_2}$) according to the coordinates of the M point generating the halide environment at the B′ site.

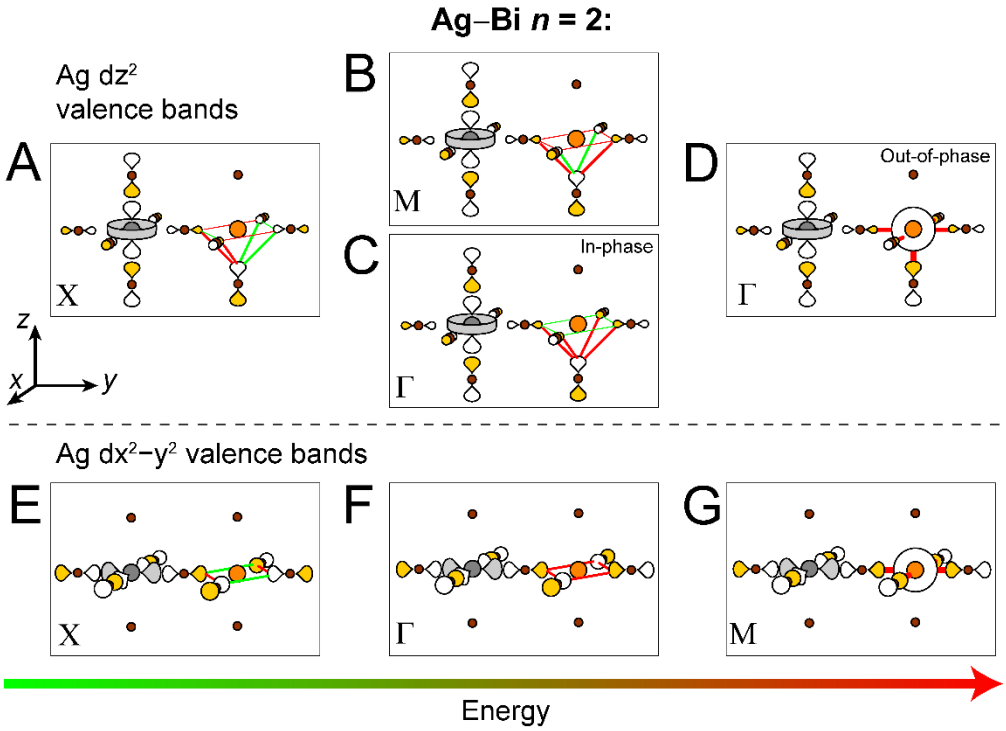

Figure S17. LCAO representations of the Ag dz^2 (A-D) and $dx^2{-}y^2$ (E-G) VBs of the $n = 2$ Ag–Bi structure at M, X, and Γ ranked in order of increasing energy from left to right. These depictions were used to predict the dispersion of the Ag–Bi $n = 2$ VBs given in main text Figure 10. The bonding and antibonding interactions at the B′ site are shown as green and red lines, respectively, and the thickness of each line corresponds to the strength of the interaction. Gray and orange spheres represent Ag and Bi atoms, respectively. Halide p orbital lobes are scaled to represent approximate relative electron densities. See Section S5.2.1 for a discussion of why the representations in B and C are considered isoenergetic.

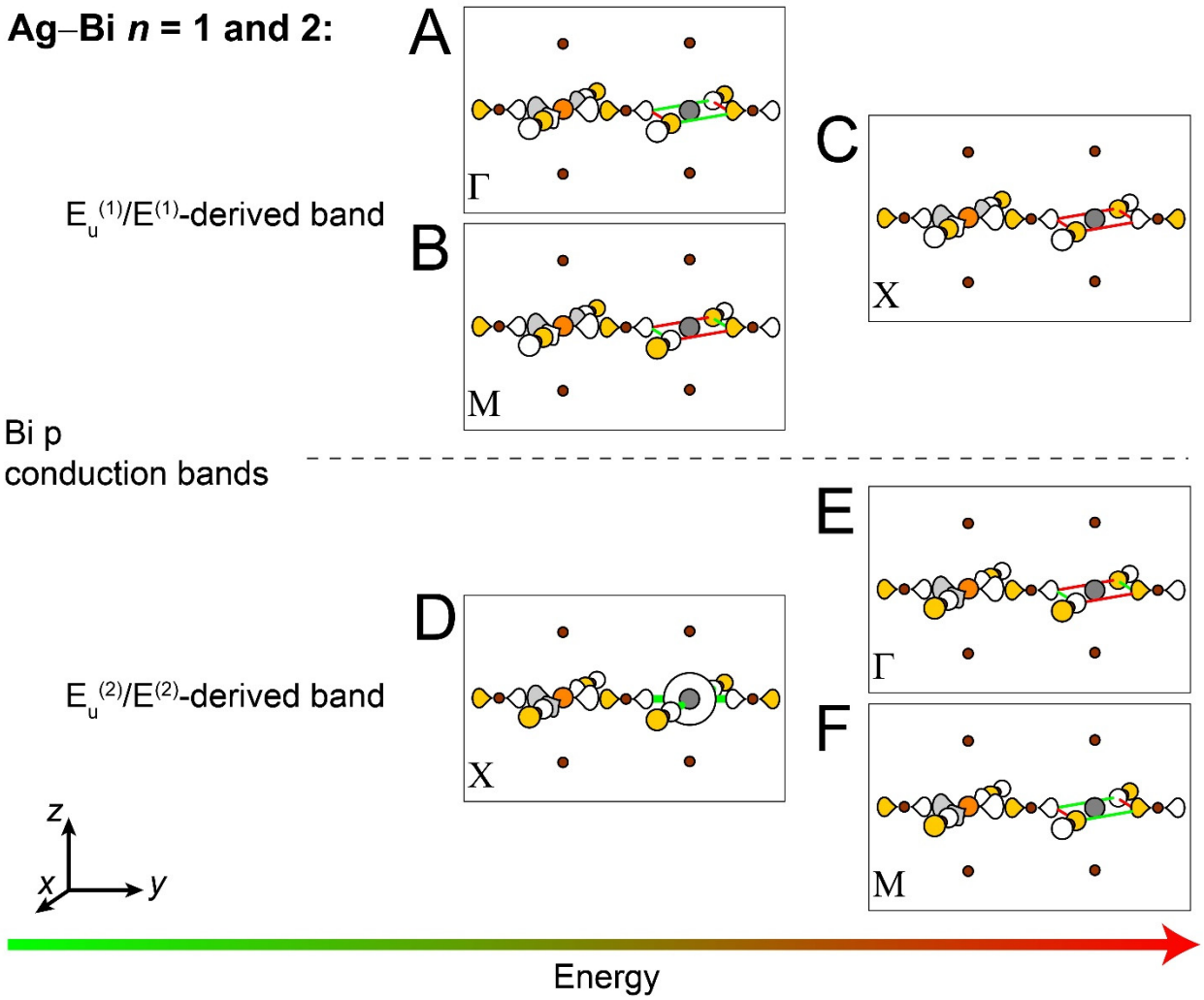

Figure S18. LCAO representations of the Bi p-based CBs of the 2D Ag–Bi structures at M, X, and Γ ranked in order of increasing energy from left to right. The $E_u^{(1)}/E^{(1)}$ (A-C) and $E_u^{(2)}/E^{(2)}$ (D-F) SALCs generate separate bands and are shown separately. These representations apply to both the n = 1 and 2 cases since the $E_u^{(1)}$ and $E_u^{(2)}$ derived halide Bloch waves for the n = 1 lattice are identical to the $E^{(1)}$ and $E^{(2)}$ derived halide Bloch waves of the n = 2 lattice (main text Figure 6). These depictions were used to predict the dispersion of the Ag–Bi n = 1 and 2 CBs given in main text Figure 8 and Figure 10. The bonding and antibonding interactions at the B′ site are shown as green and red lines, respectively, and the thickness of each line corresponds to the strength of the interaction. Gray and orange spheres represent Ag and Bi atoms, respectively. Halide p orbital lobes are scaled to represent approximate relative electron densities.

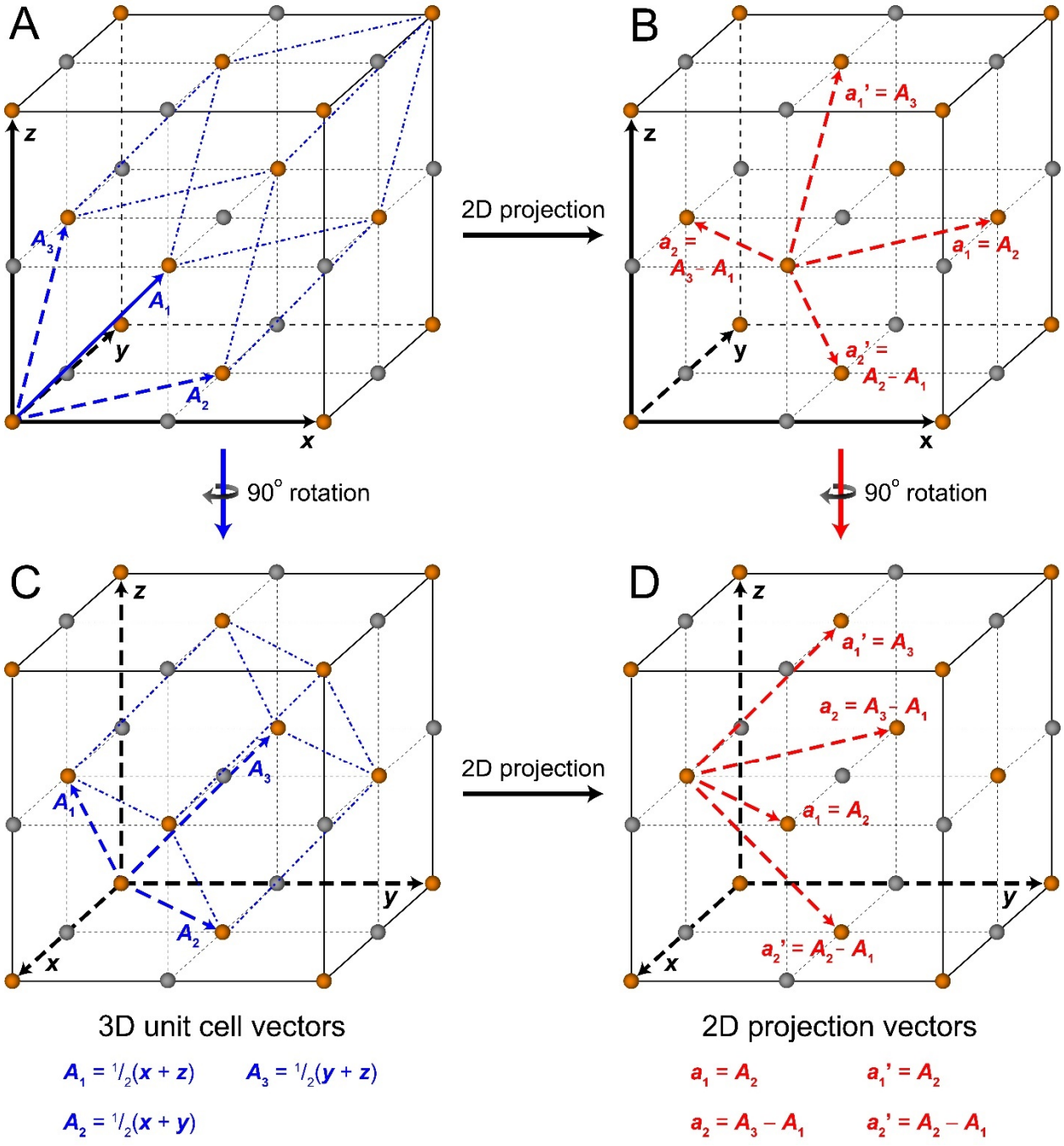

Figure S19. The B and B′ sites (gray and orange spheres) of the 3D double perovskite lattice adopt a rock-salt ordering. The primitive rhombohedral unit cell of this lattice is described by the unit cell vectors $\boldsymbol{A_1}$, $\boldsymbol{A_2}$, and $\boldsymbol{A_3}$ (A). These rhombohedral unit cell vectors can be projected onto the *xy* and *yz* planes (B), yielding two pairs of vectors ($\boldsymbol{a_1}$, $\boldsymbol{a_2}$, and $\boldsymbol{a_1'}$, $\boldsymbol{a_2'}$) that describe translations in these 2D planes which make it easier to visualize the translational symmetry of the 3D double perovskite lattice. These are the vectors used in main text Figure 11. The diagrams in C and D represent 90° rotations of those in A and B, respectively, to show the orientation of these vectors used in the main text. Note that halide anions and A site cations are omitted from these simplified diagrams.

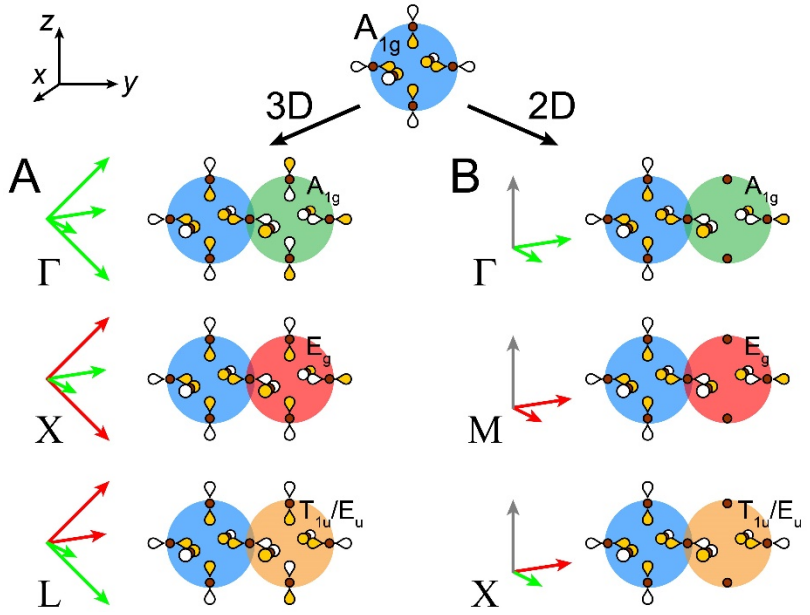

Figure S20. Halide Bloch waves derived from the A_{1g} SALC of the 3D lattice according to the translational symmetry rules of the three high-symmetry *k*-points of the 3D (A) and 2D (B) perovskite lattices. The colored circles behind each B′ site indicate the symmetry of the halide p orbital environment generated there (green = A_{1g}, yellow = T_{1u}/E_u, red = E_g). For this starting SALC, equivalent sets of Bloch waves are obtained in the 3D and 2D cases (i.e., the same symmetry of halide p orbitals is produced at the B′ site by the 3D and 2D translational symmetry rules) indicating that bands derived from B-site metal s orbitals will follow the same pattern of dispersion in the 3D and 2D lattices (assuming no involvement of B′-site metal d orbitals, see Section S8). The relative size of p orbitals is kept uniform in these diagrams for simplicity.

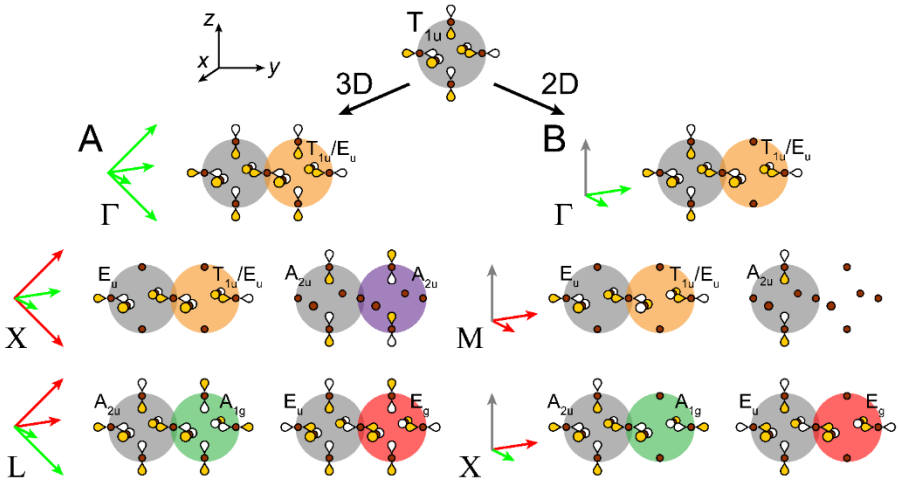

Figure S21. Halide Bloch waves derived from one of the three degenerate T_{1u} SALCs of the 3D lattice according to the translational symmetry rules of the three high-symmetry *k*-points of the 3D (A) and 2D (B) perovskite lattices. The colored circles behind each B′ site indicate the symmetry of the halide p orbital environment generated there (green = A_{1g}, yellow = T_{1u}/E_u, red = E_g, purple = A_{2u}, blank = no halide orbitals at the B′ site). For this starting SALC, equivalent sets of Bloch waves are obtained in the 3D and 2D cases (i.e., the same symmetry of halide p orbitals is produced at the B′ site by the 3D and 2D translational symmetry rules) indicating that bands derived from B-site metal p orbitals will follow the same pattern of dispersion in the 3D and 2D lattices (in the absence of SOC effects, see Section S4, and assuming no involvement of B′-site metal d orbitals, see Section S8). Note that the splitting of the three degenerate 3D T_{1u} SALCs at the X and L points, and into E_u and A_{2u} SALCs in the 2D case, does not affect this result (see Section S7). The relative size of p orbitals is kept uniform in these diagrams for simplicity.

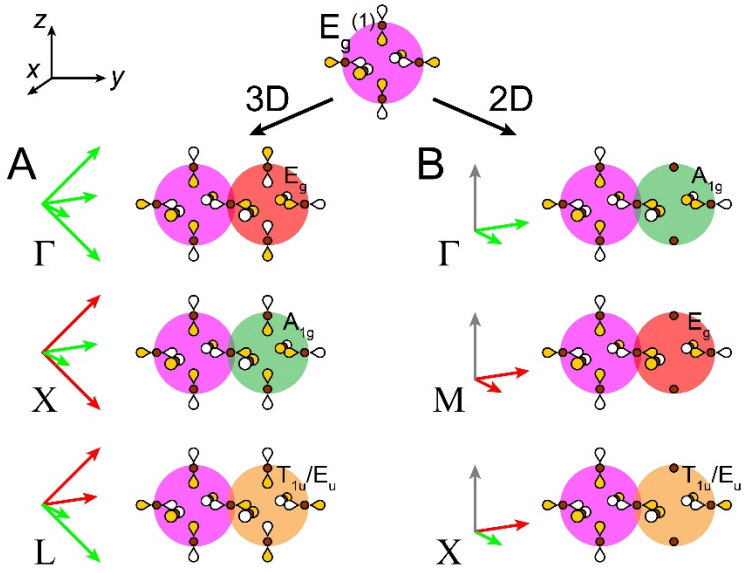

Figure S22. Halide Bloch waves derived from the $E_g^{(1)}$ SALC of the 3D lattice according to the translational symmetry rules of the three high-symmetry *k*-points of the 3D (A) and 2D (B) perovskite lattices. The colored circles behind each B′ site indicate the symmetry of the halide p orbital environment generated there (green = A_{1g}, yellow = T_{1u}/E_u, red = E_g). For this starting SALC, 3D and 2D translational symmetry *do not* generate equivalent sets of Bloch waves (i.e., in some cases 3D and 2D translational symmetry generate halide p orbital environments at the B′ site with different symmetries), indicating that bands derived from B-site metal dz^2 orbitals will *not* follow the same pattern of dispersion in the 3D and 2D lattices. The relative size of p orbitals is kept uniform in these diagrams for simplicity.

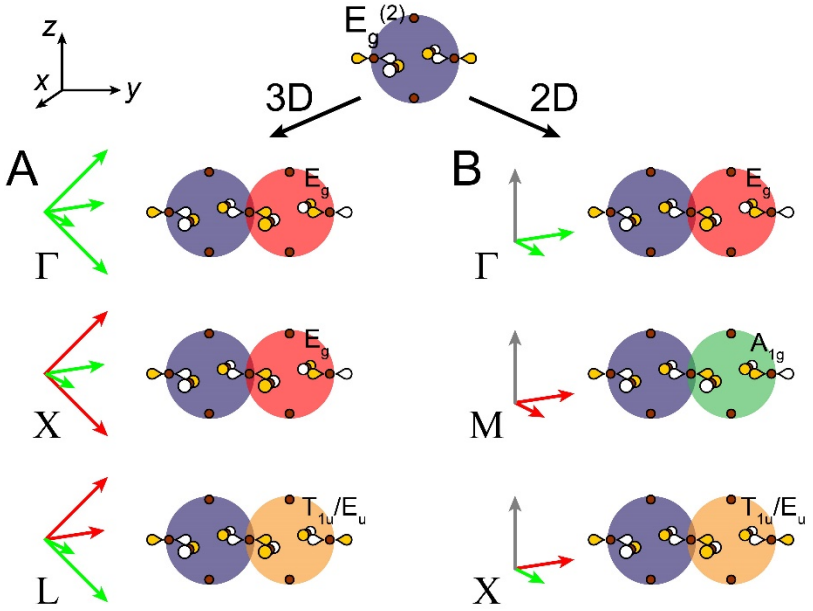

Figure S23. Halide Bloch waves derived from the $E_g^{(2)}$ SALC of the 3D lattice according to the translational symmetry rules of the three high-symmetry *k*-points of the 3D (A) and 2D (B) perovskite lattices. The colored circles behind each B′ site indicate the symmetry of the halide p orbital environment generated there (green = A_{1g}, yellow = T_{1u}/E_u, red = E_g). For this starting SALC, 3D and 2D translational symmetry *do not* generate equivalent sets of Bloch waves (i.e., in some cases 3D and 2D translational symmetry generate halide p orbital environments at the B′ site with different symmetries), indicating that bands derived from B-site metal $dx^2–y^2$ orbitals will *not* follow the same pattern of dispersion in the 3D and 2D lattices.

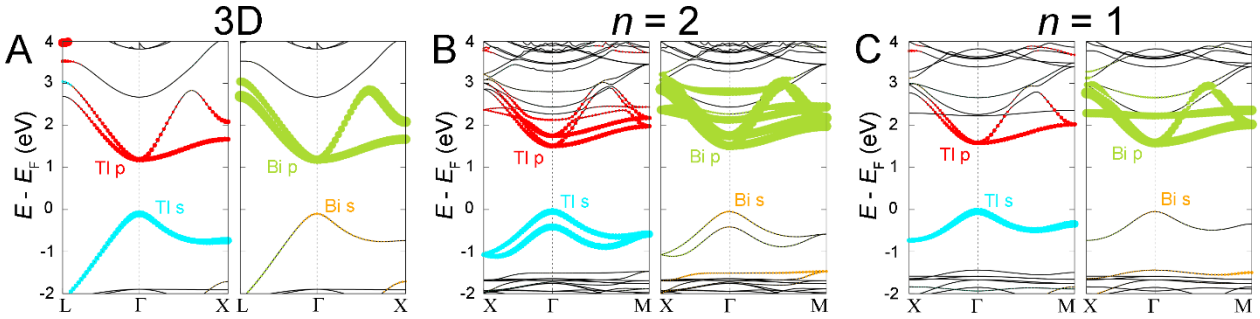

Figure S24. Band structure of 3D $(CH_3NH_3)_2TlBiBr_6$ (A) and the undistorted model $n = 2$ (B) and $n = 1$ (C) derivatives calculated with SOC. All three structures show analogous patterns of band dispersion, as expected for a double perovskite composition where the band edges have only metal s and p character.

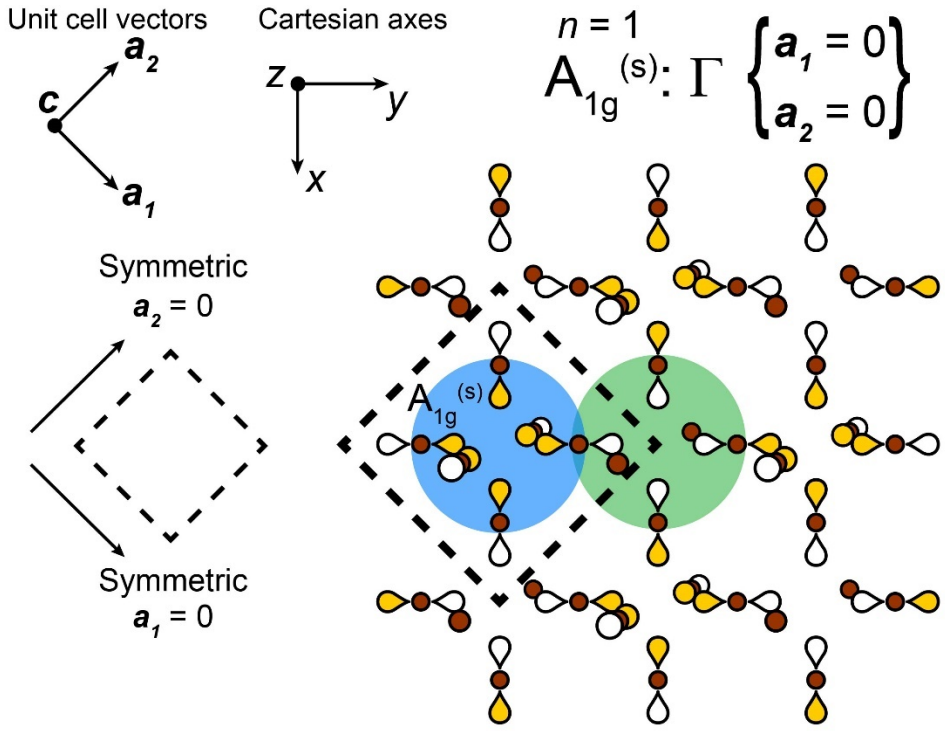

Figure S25. Derivation of the halide Bloch wave at Γ for the $n = 1$ $A_{1g}^{(s)}$ SALC (blue circle).

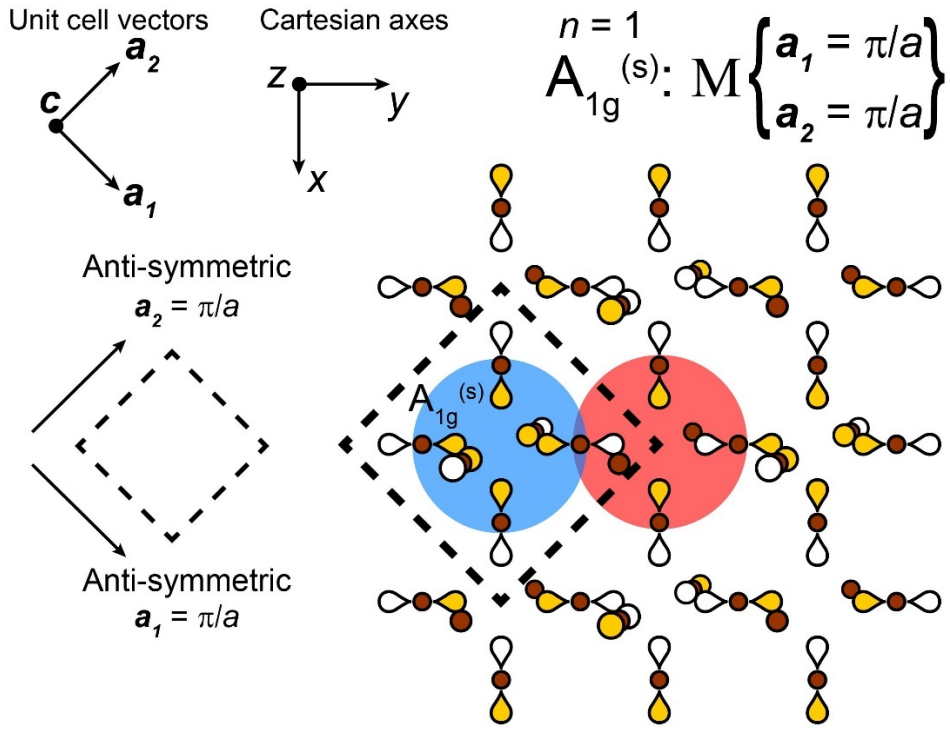

Figure S26. Derivation of the halide Bloch wave at M for the $n = 1$ $A_{1g}^{(s)}$ SALC (blue circle).

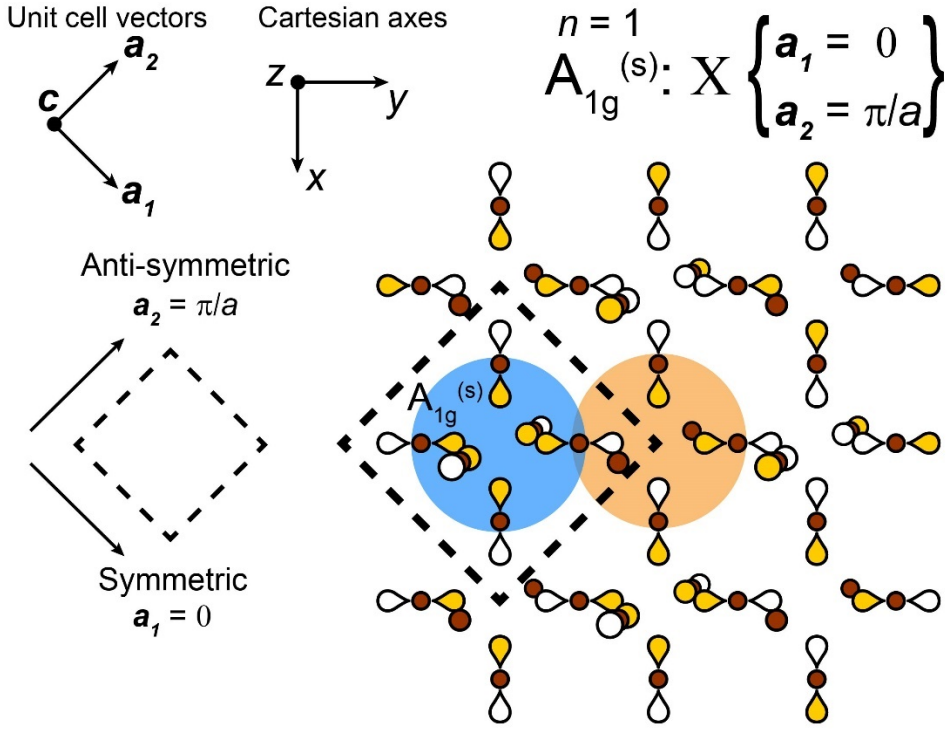

Figure S27. Derivation of the halide Bloch wave at X for the $n = 1$ $A_{1g}^{(s))}$ SALC (blue circle).

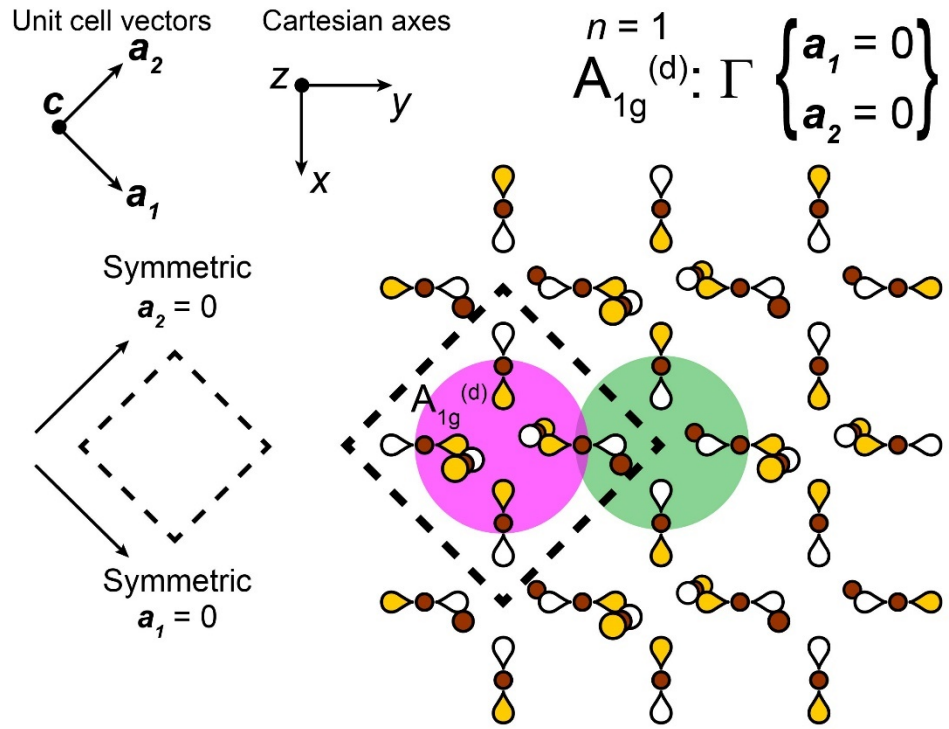

Figure S28. Derivation of the halide Bloch wave at Γ for the $n = 1$ $A_{1g}^{(d)}$ SALC (magenta circle).

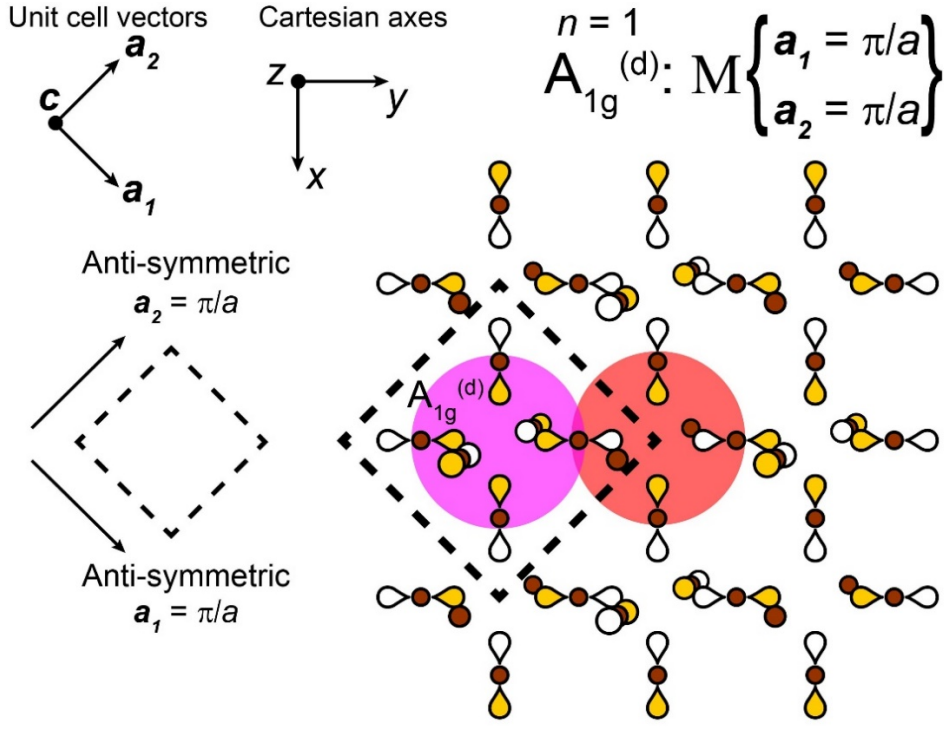

Figure S29. Derivation of the halide Bloch wave at M for the $n = 1$ $A_{1g}^{(d)}$ SALC (magenta circle).

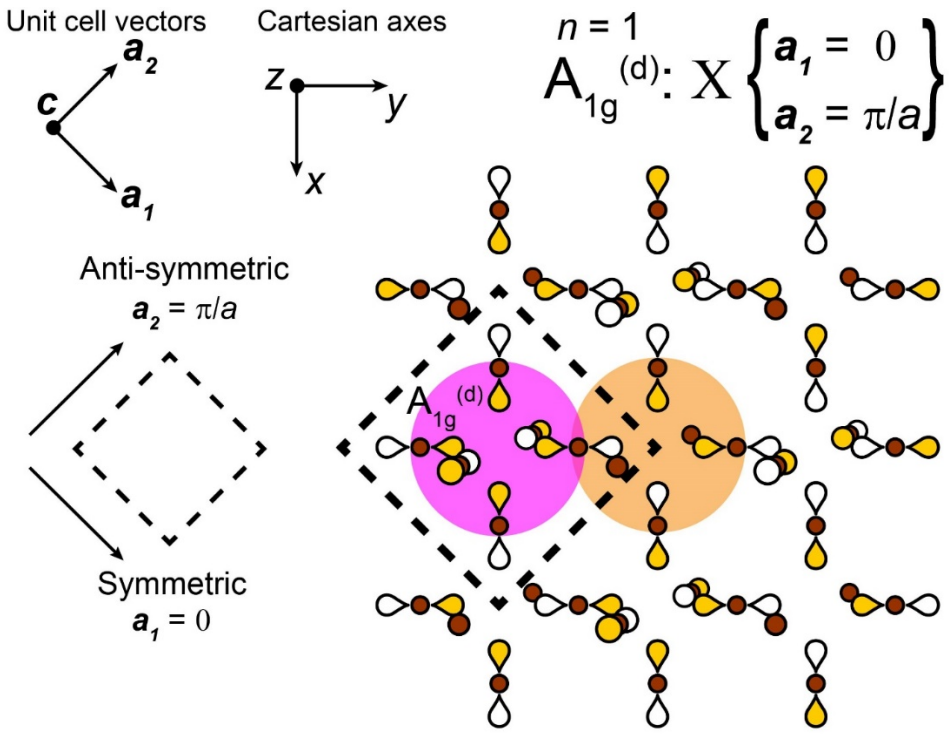

Figure S30. Derivation of the halide Bloch wave at X for the $n = 1$ $A_{1g}^{(d)}$ SALC (magenta circle).

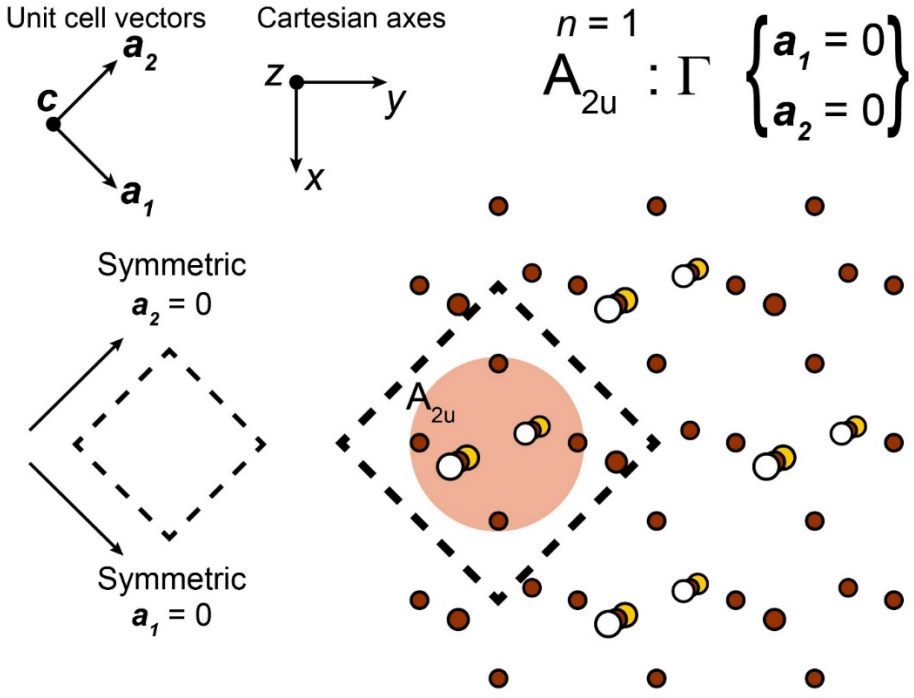

Figure S31. Derivation of the halide Bloch wave at Γ for the $n = 1$ A_{2u} SALC (tan circle).

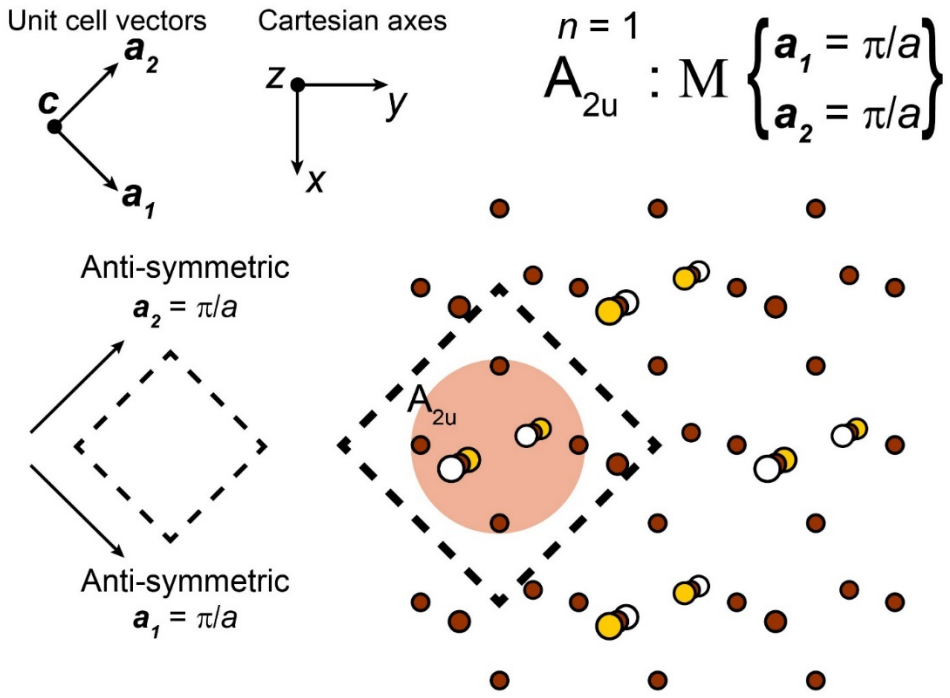

Figure S32. Derivation of the halide Bloch wave at M for the $n = 1$ A_{2u} SALC (tan circle).

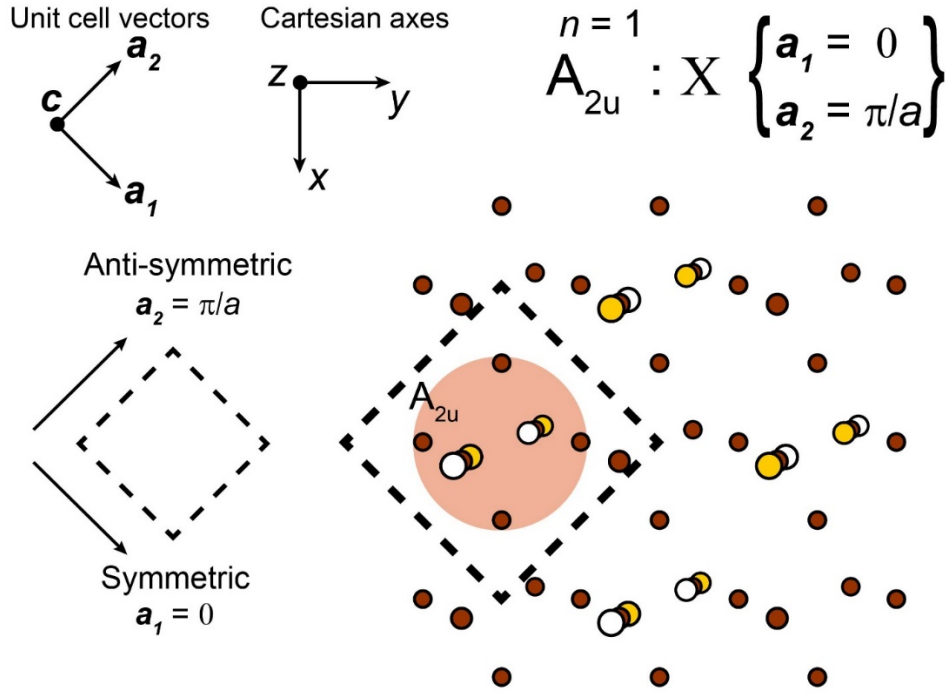

Figure S33. Derivation of the halide Bloch wave at X for the $n = 1$ A_{2u} SALC (tan circle).

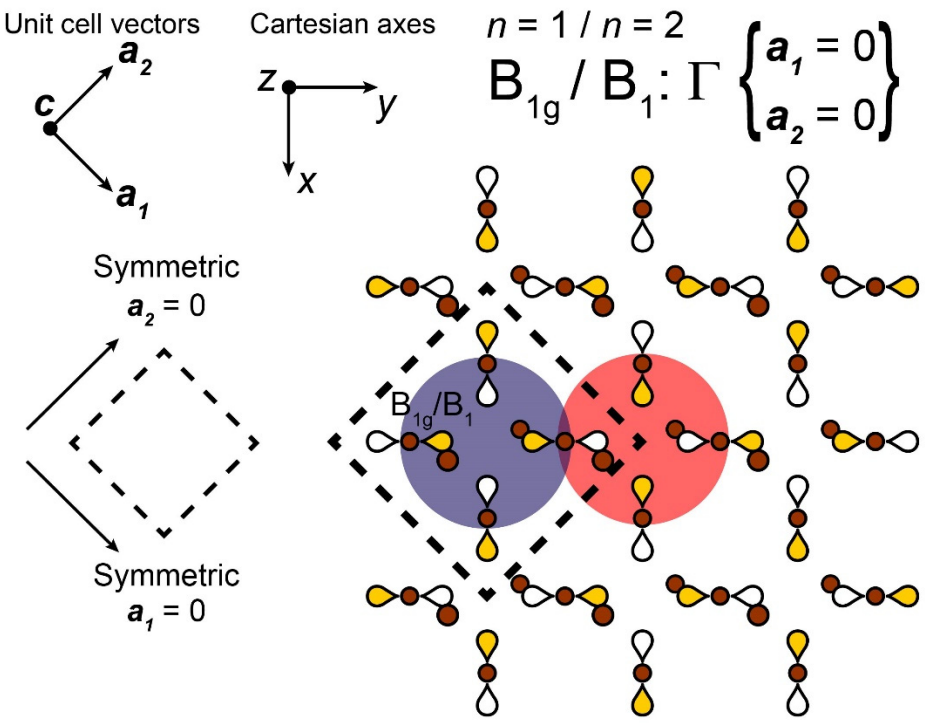

Figure S34. Derivation of the halide Bloch wave at Γ for the (equivalent) $n = 1$ B_{1g} and $n = 2$ B_1 SALCs (navy circle).

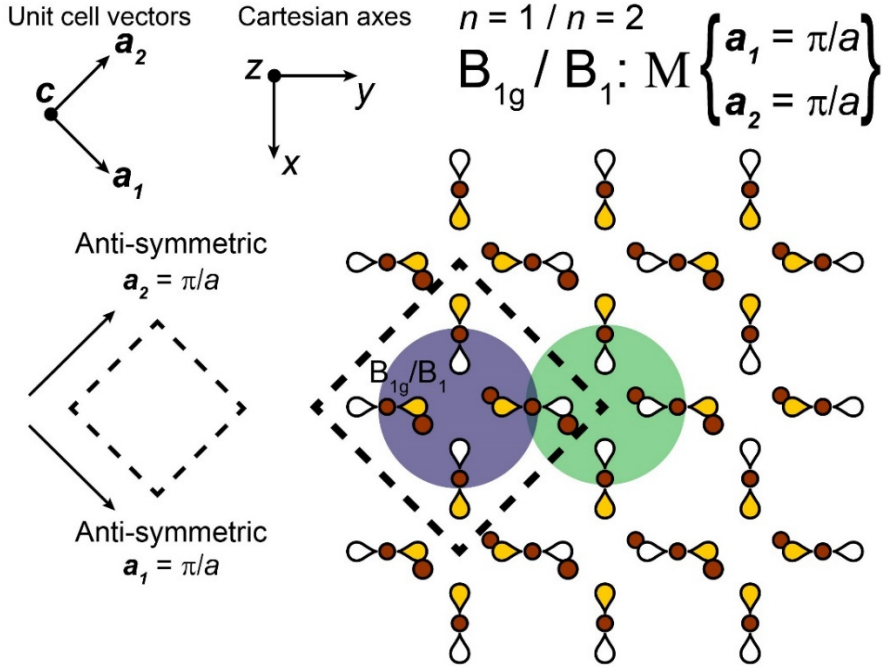

Figure S35. Derivation of the halide Bloch wave at M for the (equivalent) $n = 1$ B_{1g} and $n = 2$ B_1 SALCs (navy circle).

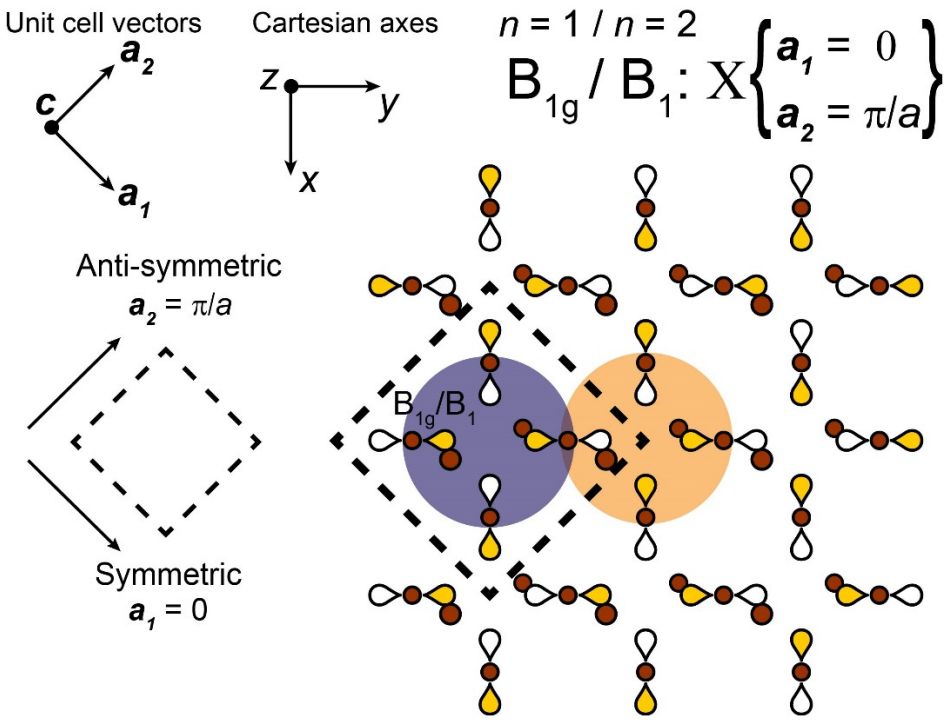

Figure S36. Derivation of the halide Bloch wave at X for the (equivalent) $n = 1$ B_{1g} and $n = 2$ B_1 SALCs (navy circle).

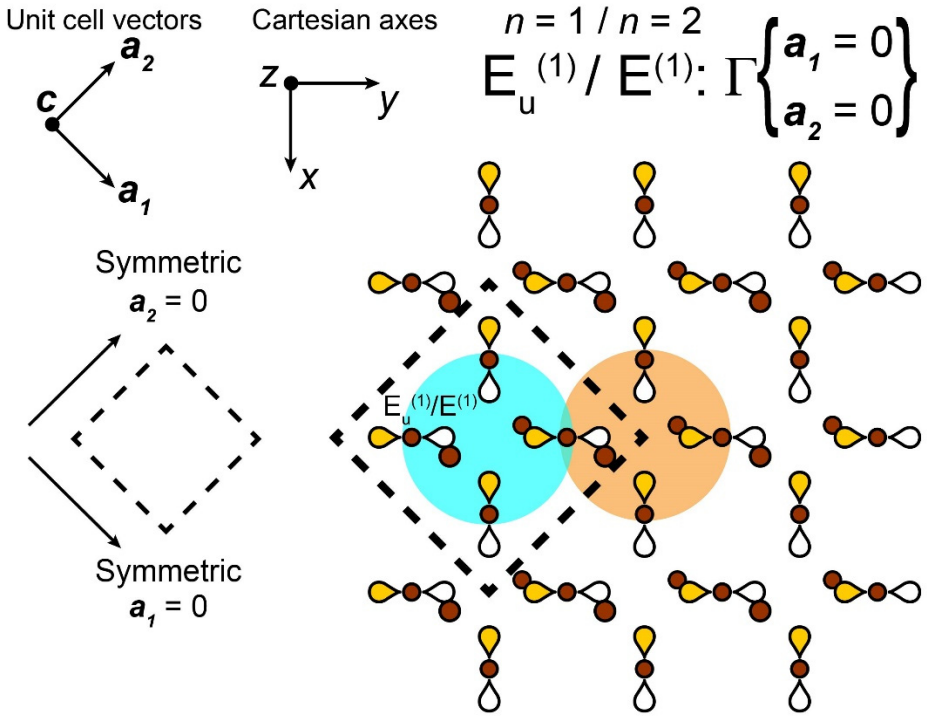

Figure S37. Derivation of the halide Bloch wave at Γ for the (equivalent) $n = 1$ $E_u^{(1)}$ and $n = 2$ $E^{(1)}$ SALCs (turquoise circle).

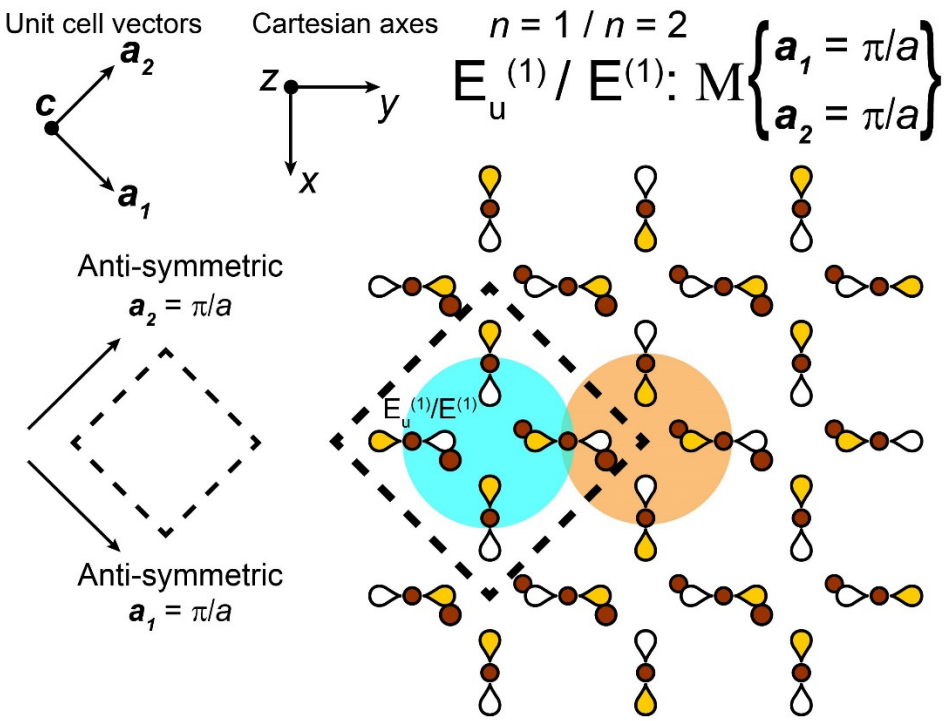

Figure S38. Derivation of the halide Bloch wave at M for the (equivalent) $n = 1$ $E_u^{(1)}$ and $n = 2$ $E^{(1)}$ SALCs (turquoise circle).

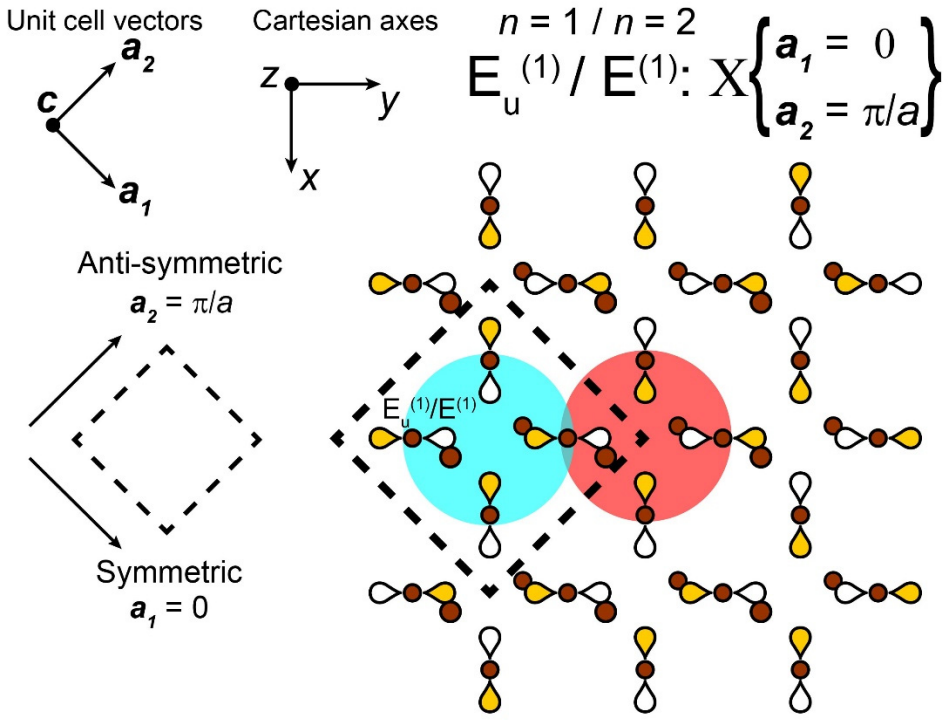

Figure S39. Derivation of the halide Bloch wave at X for the (equivalent) $n = 1$ $E_u^{(1)}$ and $n = 2$ $E^{(1)}$ SALCs (turquoise circle).

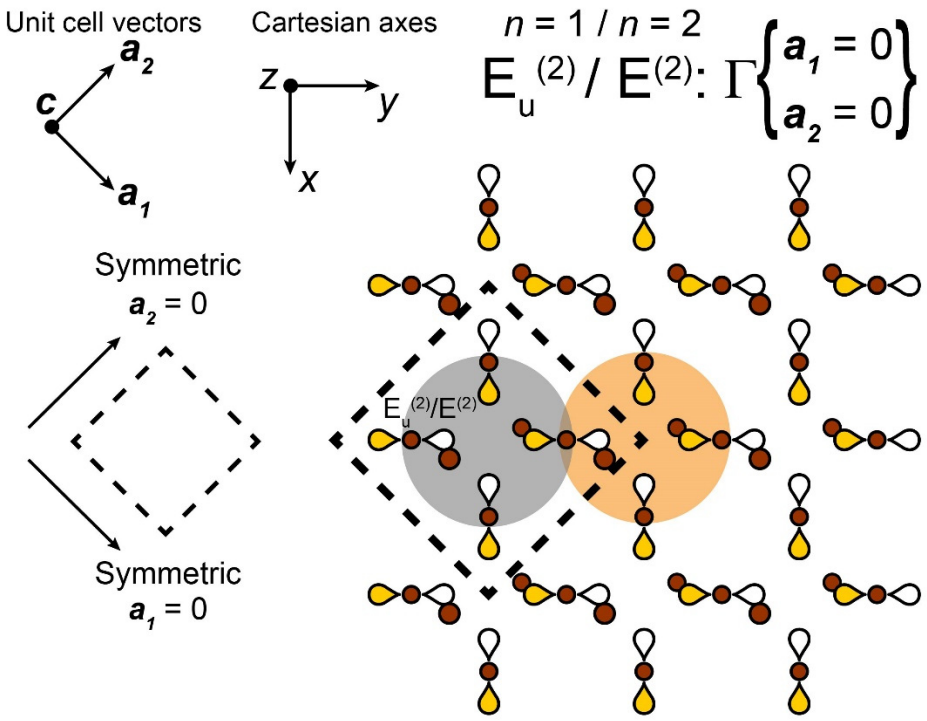

Figure S40. Derivation of the halide Bloch wave at Γ for the (equivalent) $n = 1$ $E_u^{(2)}$ and $n = 2$ $E^{(2)}$ SALCs (gray circle).

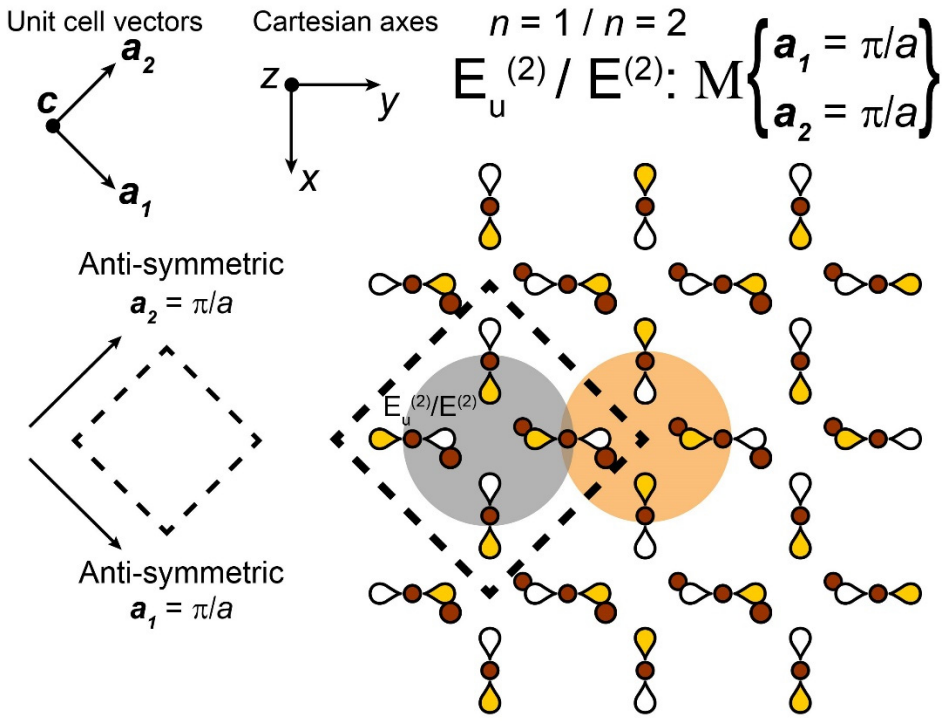

Figure S41. Derivation of the halide Bloch wave at M for the (equivalent) $n = 1$ $E_u^{(2)}$ and $n = 2$ $E^{(2)}$ SALCs (gray circle).

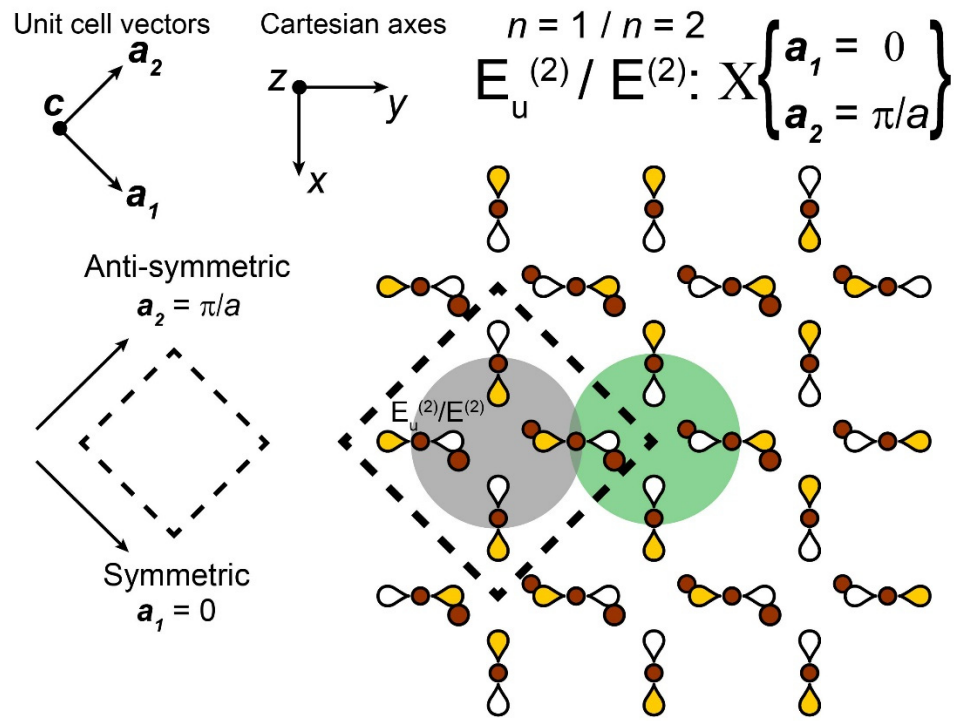

Figure S42. Derivation of the halide Bloch wave at X for the (equivalent) $n = 1$ $E_u^{(2)}$ and $n = 2$ $E^{(2)}$ SALCs (gray circle).

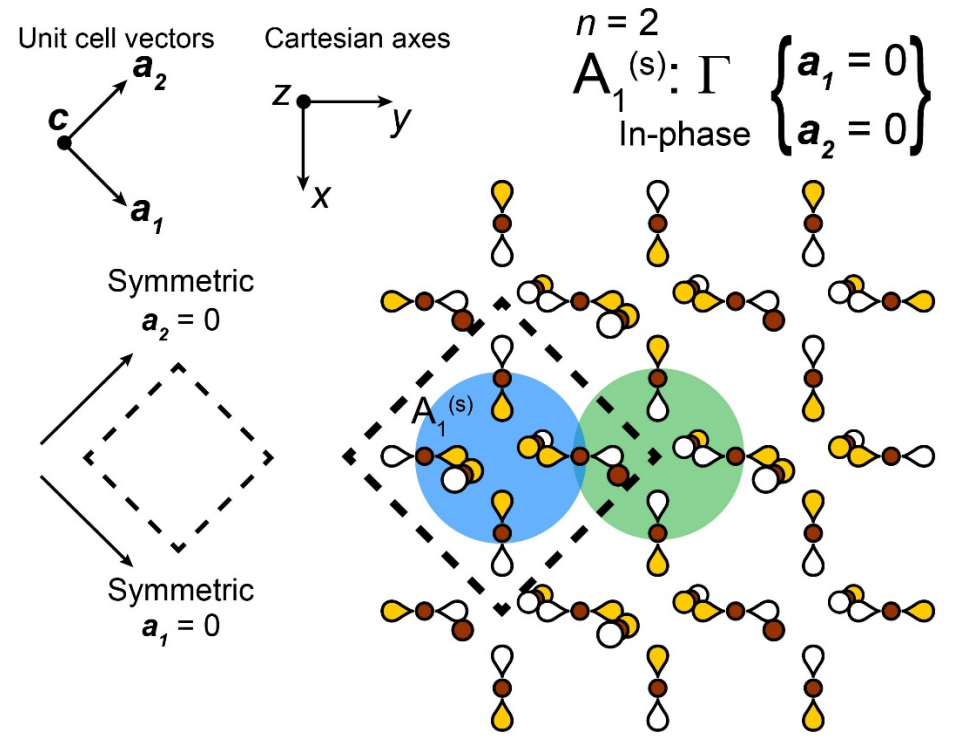

Figure S43. Derivation of the halide Bloch wave at Γ for the in-phase combination of $n = 2$ $A_1^{(s)}$ SALCs (blue circle).

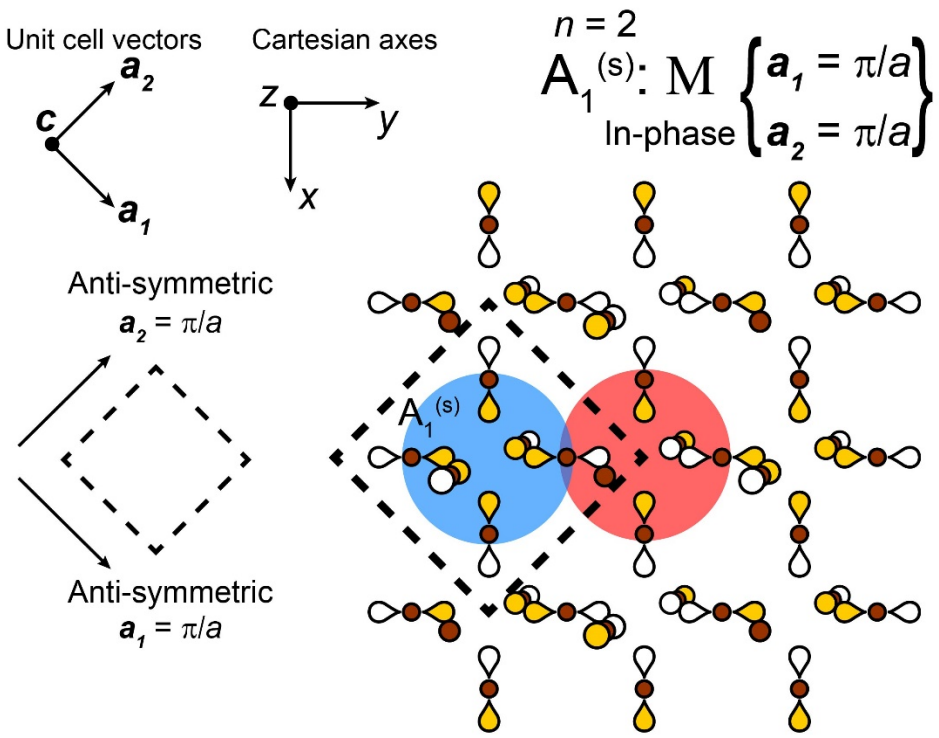

Figure S44. Derivation of the halide Bloch wave at M for the in-phase combination of $n = 2$ $A_1^{(s)}$ SALCs (blue circle).

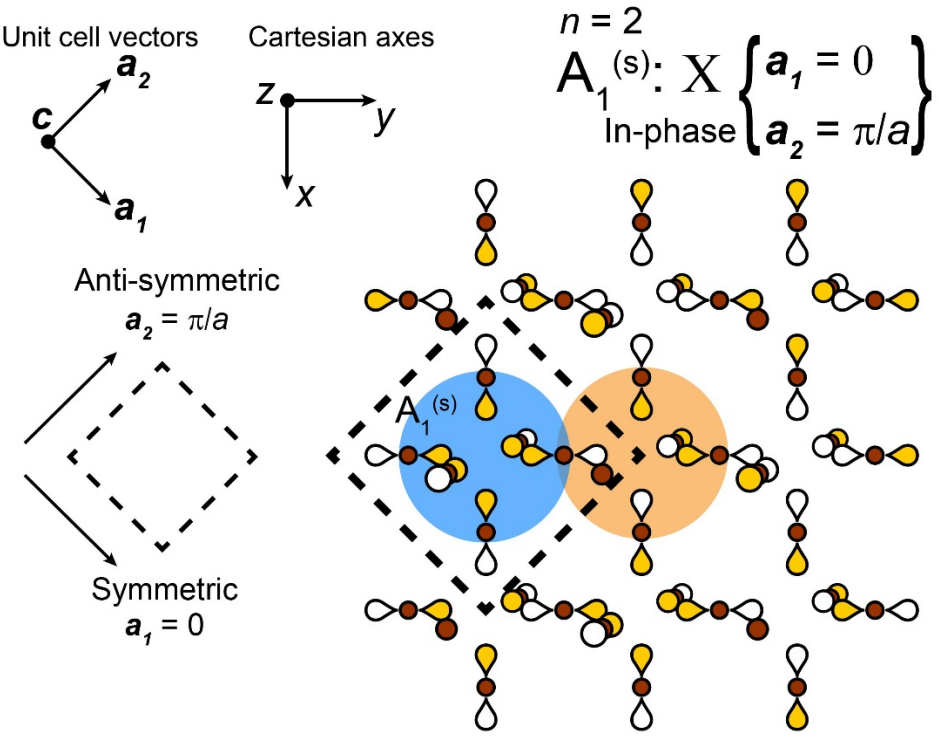

Figure S45. Derivation of the halide Bloch wave at X for the in-phase combination of $n = 2$ $A_1^{(s)}$ SALCs (blue circle).

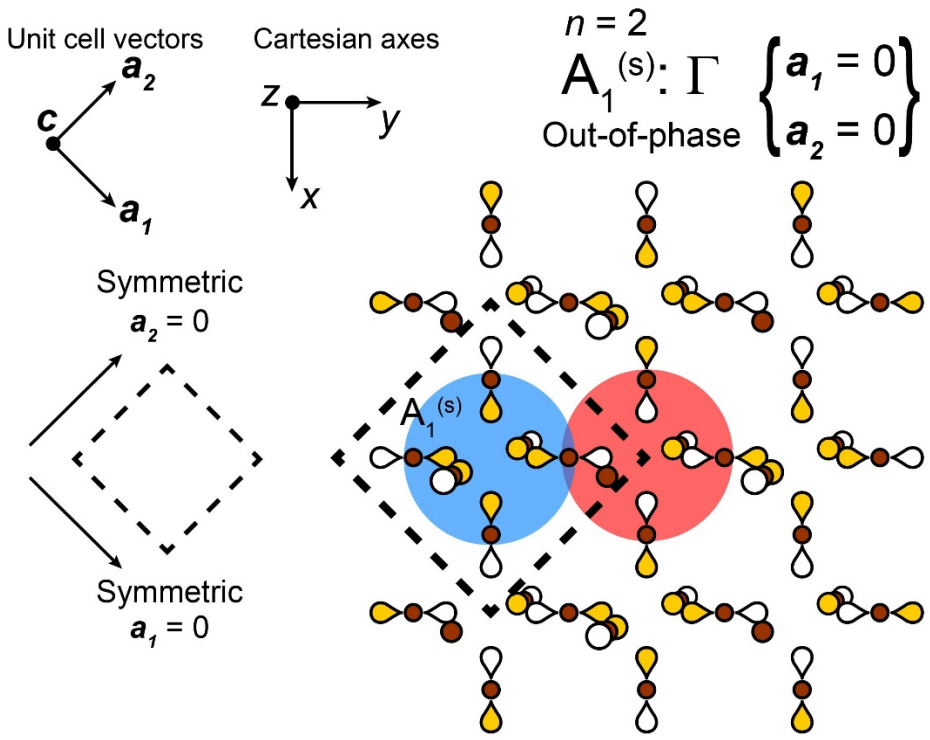

Figure S46. Derivation of the halide Bloch wave at Γ for the out-of-phase combination of $n = 2$ $A_1^{(s)}$ SALCs (blue circle).

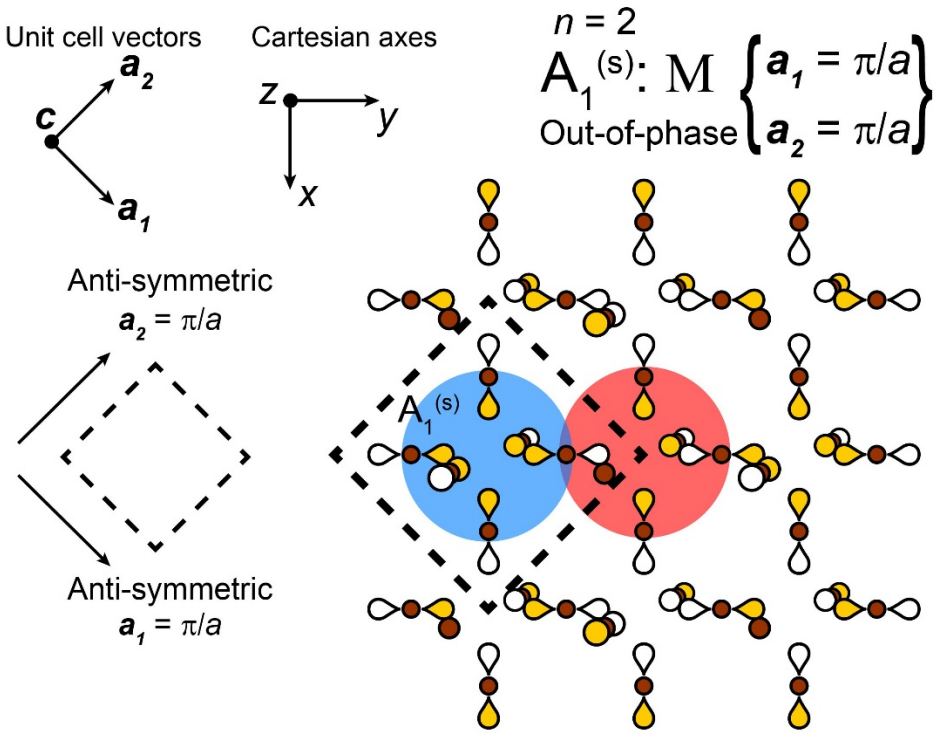

Figure S47. Derivation of the halide Bloch wave at M for the out-of-phase combination of $n = 2$ $A_1^{(s)}$ SALCs (blue circle).

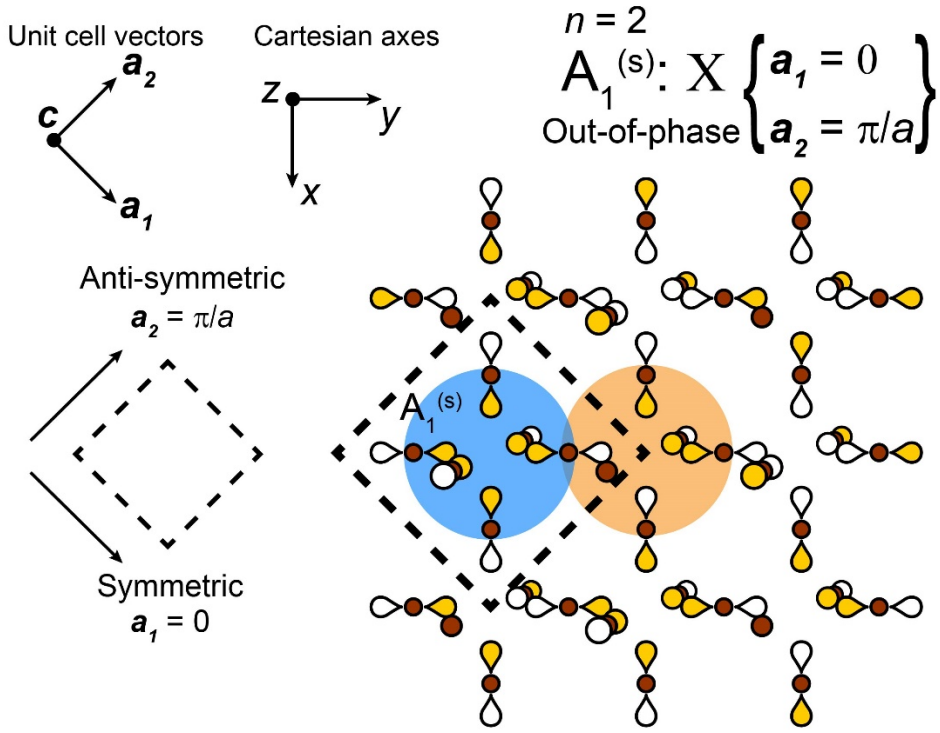

Figure S48. Derivation of the halide Bloch wave at X for the out-of-phase combination of $n = 2$ $A_1^{(s)}$ SALCs (blue circle).

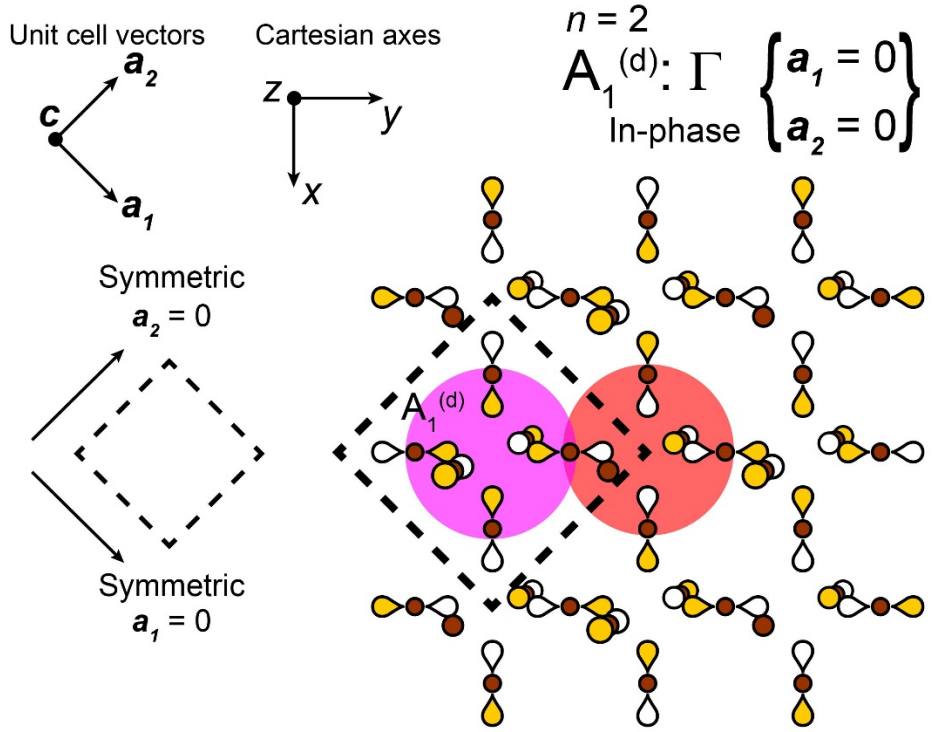

Figure S49. Derivation of the halide Bloch wave at Γ for the in-phase combination of $n = 2$ $A_1^{(d)}$ SALCs (magenta circle).

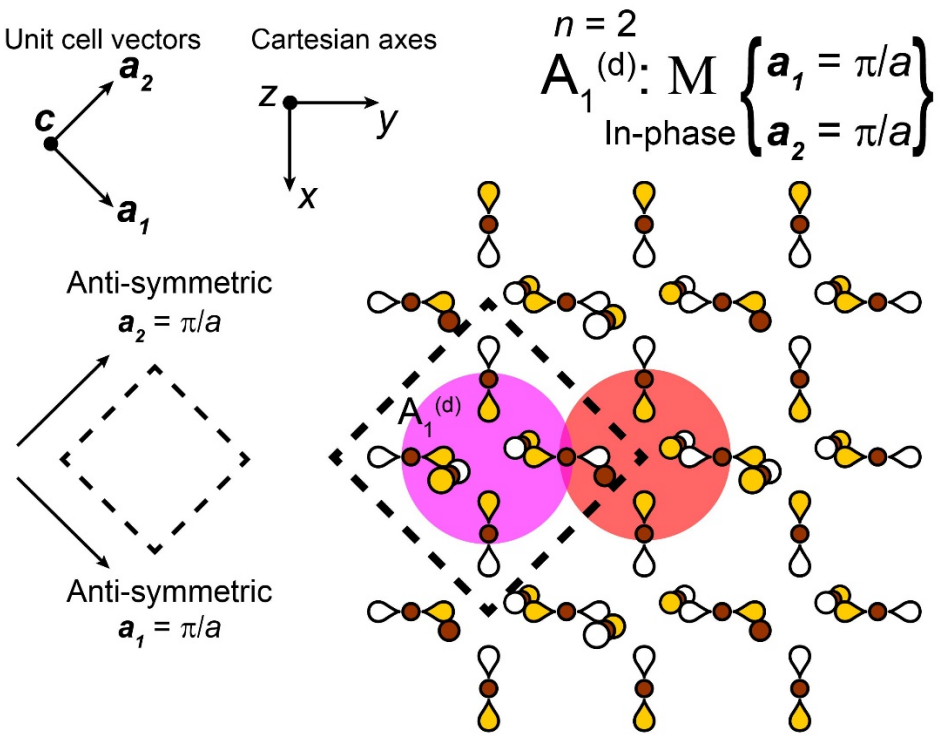

Figure S50. Derivation of the halide Bloch wave at M for the in-phase combination of $n = 2$ $A_1^{(d)}$ SALCs (magenta circle).

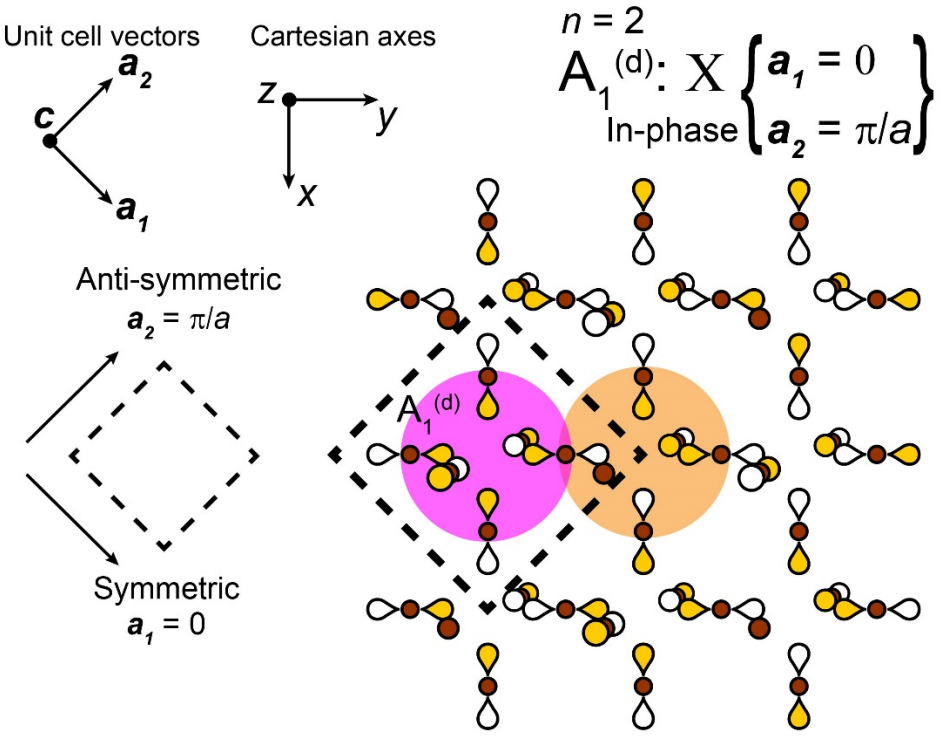

Figure S51. Derivation of the halide Bloch wave at X for the in-phase combination of $n = 2$ $A_1^{(d)}$ SALCs (magenta circle).

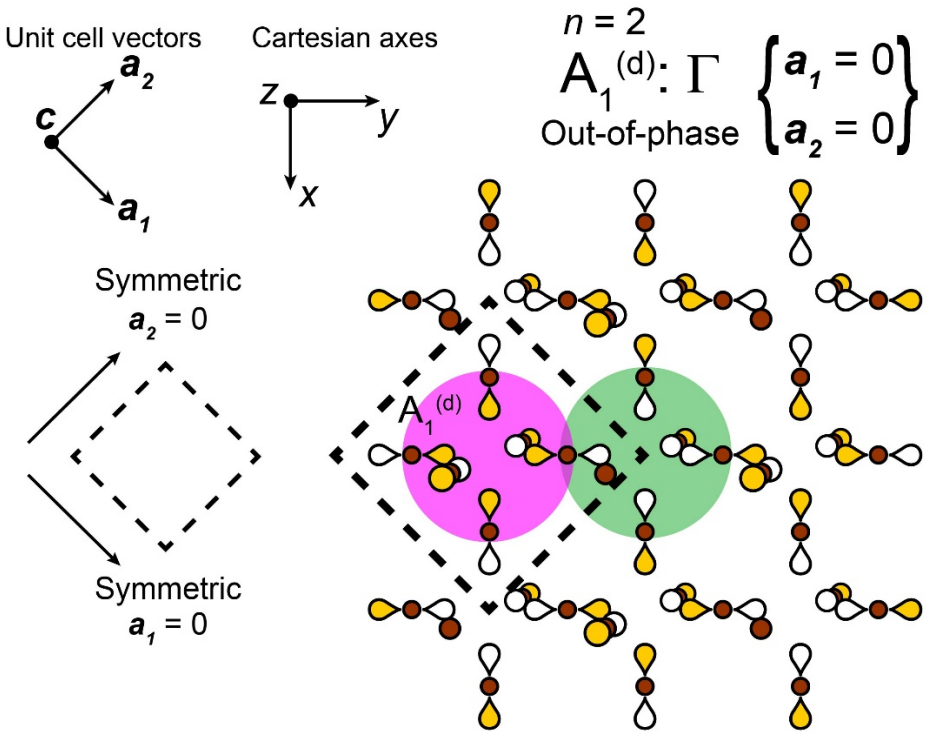

Figure S52. Derivation of the halide Bloch wave at Γ for the out-of-phase combination of $n = 2$ $A_1^{(d)}$ SALCs (magenta circle).

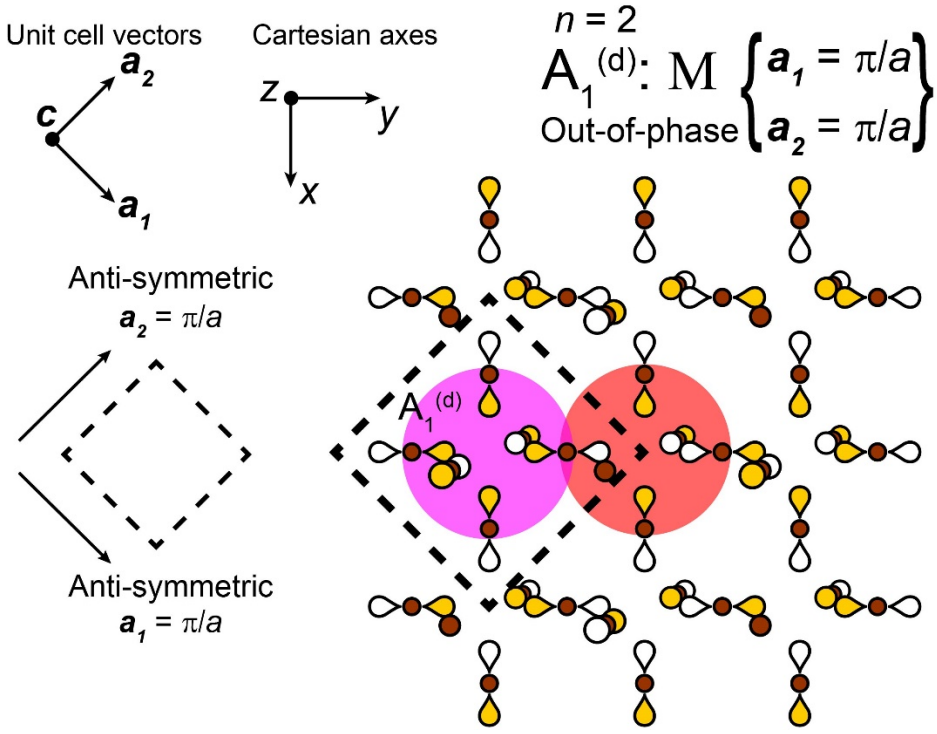

Figure S53. Derivation of the halide Bloch wave at M for the out-of-phase combination of $n = 2$ $A_1^{(d)}$ SALCs (magenta circle).

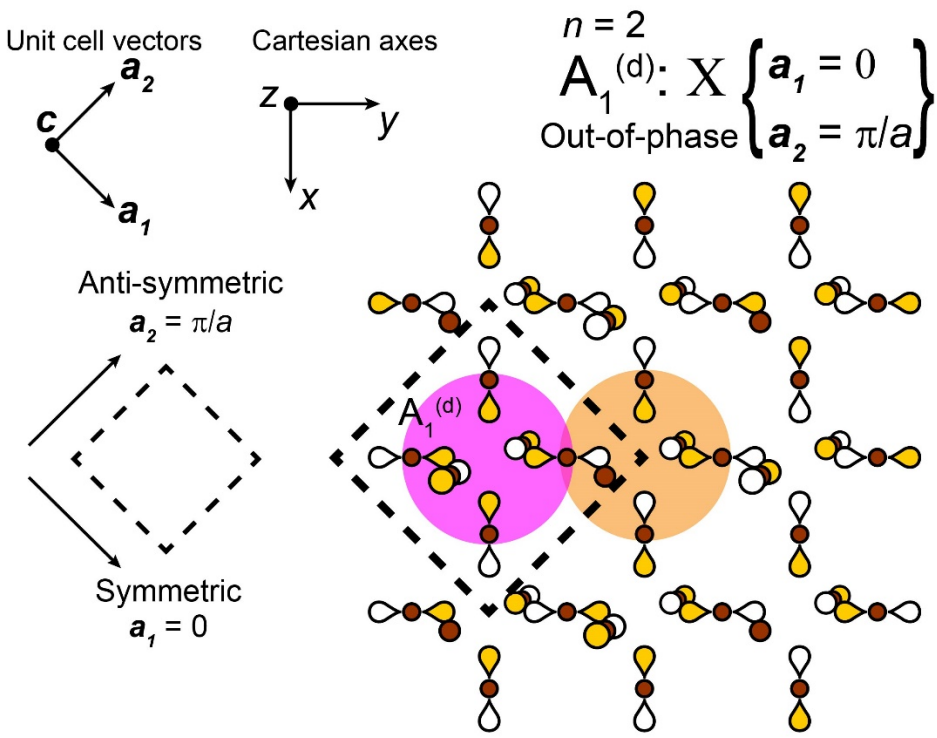

Figure S54. Derivation of the halide Bloch wave at X for the out-of-phase combination of $n = 2$ $A_1^{(d)}$ SALCs (magenta circle).

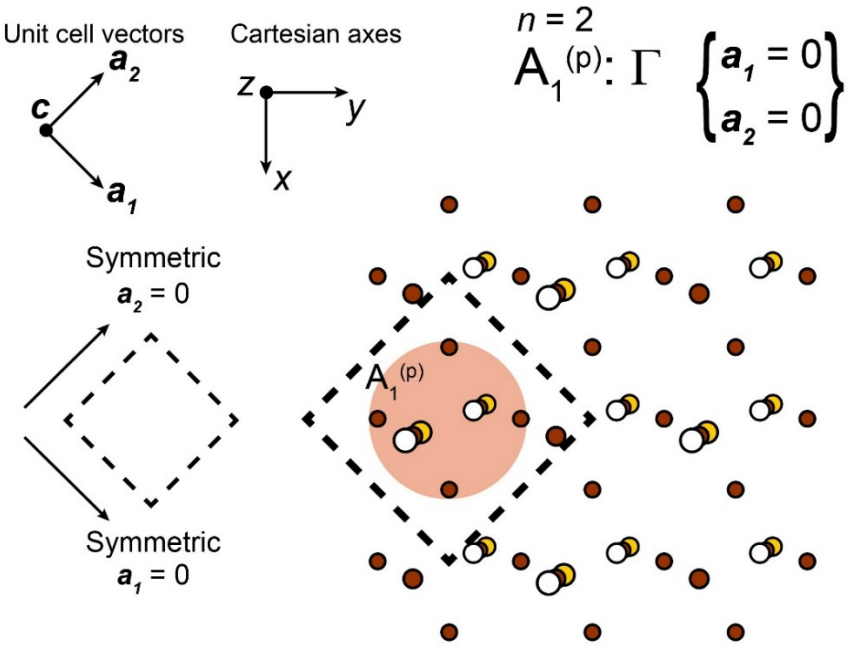

Figure S55. Derivation of the halide Bloch wave at Γ for the in-phase combination of $n = 2$ $A_1^{(p)}$ SALCs (tan circle). The Bloch wave generated from the out-of-phase combination has an identical halide environment at the B′ site and therefore is not included.

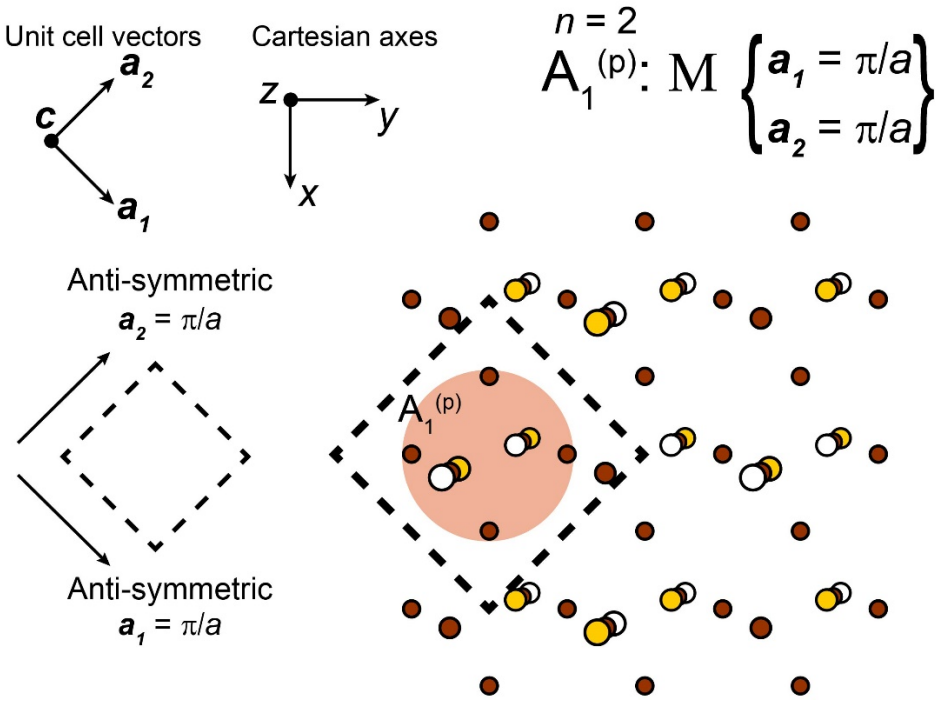

Figure S56. Derivation of the halide Bloch wave at M for the in-phase combination of $n = 2$ $A_1^{(p)}$ SALCs (tan circle). The Bloch wave generated from the out-of-phase combination has an identical halide environment at the B′ site and therefore is not included.

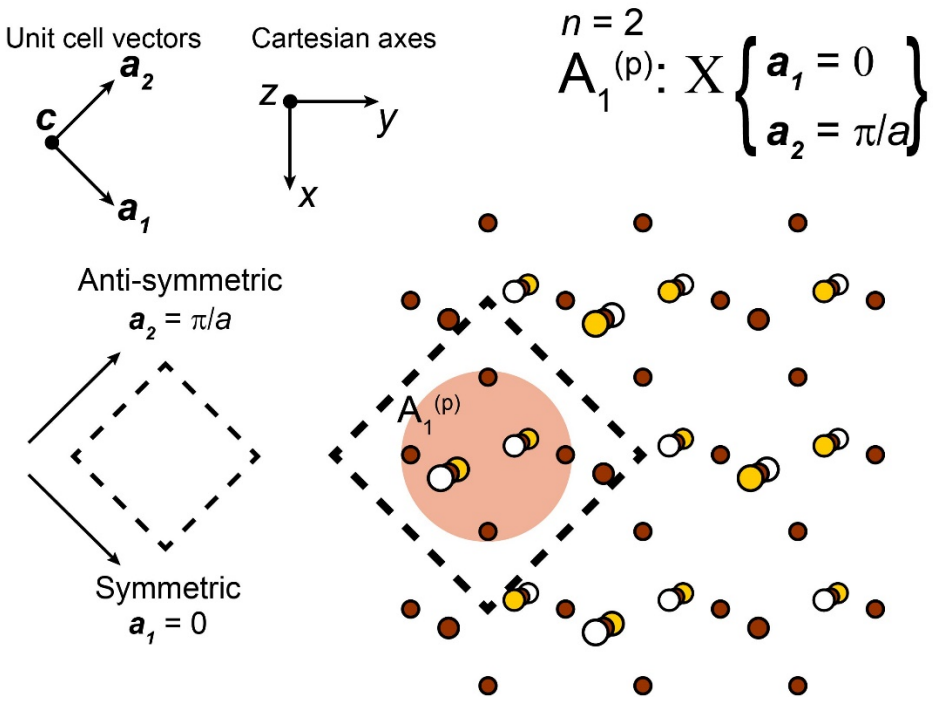

Figure S57. Derivation of the halide Bloch wave at X for the in-phase combination of $n = 2$ $A_1^{(p)}$ SALCs (tan circle). The Bloch wave generated from the out-of-phase combination has an identical halide environment at the B′ site and therefore is not included.

References

1. G. Kresse and J. Hafner, Norm-conserving and ultrasoft pseudopotentials for first-row and transition elements, *J. Phys. Condens. Matter*, 1994, **6**, 8245-8257.
2. G. Kresse and J. Furthmüller, Efficient Iterative Schemes for Ab Initio Total-Energy Calculations Using a Plane-Wave Basis Set, *Phys. Rev. B*, 1996, **54**, 11169-11186.
3. G. I. Csonka, J. P. Perdew, A. Ruzsinszky, P. H. T. Philipsen, S. Lebègue, J. Paier, O. A. Vydrov and J. G. Ángyán, Assessing the performance of recent density functionals for bulk solids, *Phys. Rev. B*, 2009, **79**, 155107.
4. G. Kresse and D. Joubert, From ultrasoft pseudopotentials to the projector augmented-wave method, *Phys. Rev. B*, 1999, **59**, 1758-1775.
5. A. H. Slavney, L. Leppert, A. Saldivar Valdes, D. Bartesaghi, T. J. Savenije, J. B. Neaton and H. I. Karunadasa, Small-Band-Gap Halide Double Perovskites, *Angew. Chem. Int. Ed.*, 2018, **57**, 12765-12770.
6. J. P. Perdew, K. Burke and M. Ernzerhof, Generalized Gradient Approximation Made Simple, *Phys. Rev. Lett.*, 1996, **77**, 3865-3868.
7. G. I. Csonka, J. P. Perdew, A. Ruzsinszky, P. H. T. Philipsen, S. Lebègue, J. Paier, O. A. Vydrov and J. G. Ángyán, Assessing the performance of recent density functionals for bulk solids, *Phys. Rev. B*, 2009, **79**, 155107.
8. A. V. Krukau, O. A. Vydrov, A. F. Izmaylov and G. E. Scuseria, Influence of the exchange screening parameter on the performance of screened hybrid functionals, *J. Chem. Phys.*, 2006, **125**, 224106.
9. A. L. W. Fetter, J. D., *Quantum Theory of Many-Particle Systems*, MacGraw-Hill, New York, 1971.
10. F. Aryasetiawan and O. Gunnarsson, The GW method, *Rep. Prog. Phys.*, 1998, **61**, 237.
11. H. Lars, On correlation effects in electron spectroscopies and the GW approximation, *J. Phys.: Condens. Matter*, 1999, **11**, R489.
12. A. H. Slavney, B. A. Connor, L. Leppert and H. I. Karunadasa, A pencil-and-paper method for elucidating halide double perovskite band structures, *Chem. Sci.*, 2019, **10**, 11041-11053.
13. W. Meng, X. Wang, Z. Xiao, J. Wang, D. B. Mitzi and Y. Yan, Parity-Forbidden Transitions and Their Impact on the Optical Absorption Properties of Lead-Free Metal Halide Perovskites and Double Perovskites, *J. Phys. Chem. Lett.*, 2017, **8**, 2999-3007.
14. M. S. Dresselhaus, G. Dresselhaus and A. Jorio, *Group Theory: Application to the Physics of Condensed Matter*, Springer, 2007.